nature

THE INTERNATIONAL WEEKLY JOURNAL OF SCIENCE

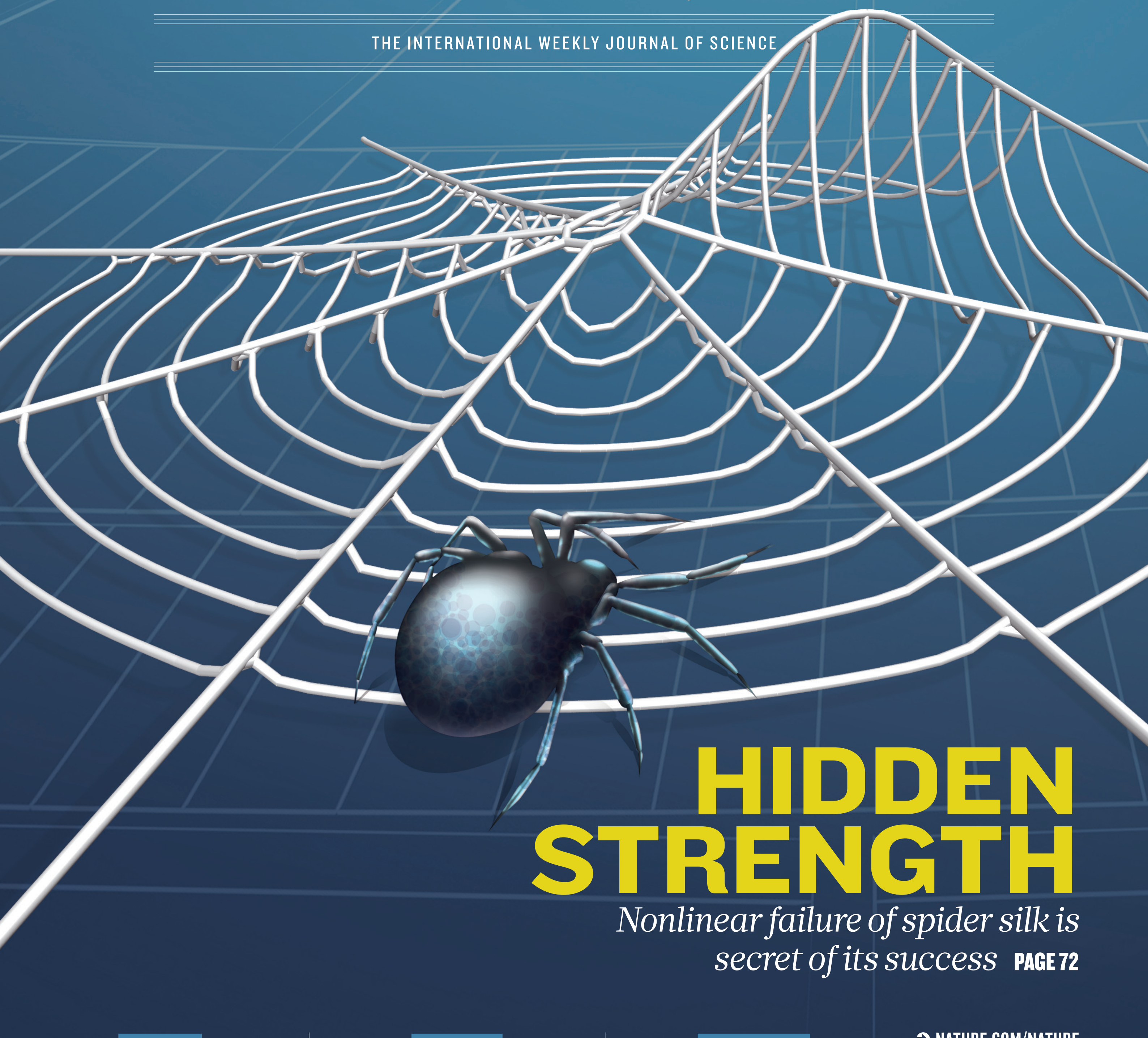

HIDDEN STRENGTH

Nonlinear failure of spider silk is secret of its success **PAGE 72**

NUTRITION

SWEET SORROW

Should sugar join tobacco and alcohol on restricted list?

PAGE 27

LITERATURE

THE OLD CURIOSITY

Science and imagination in the world of Charles Dickens

PAGE 32

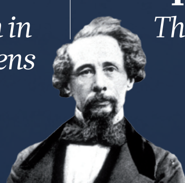

MICROBIOLOGY

RESISTANCE FIGHTERS

The rocky road to an MRSA vaccine

PAGE 23

NATURE.COM/NATURE

2 February 2012

$10.00US $12.99CAN

05

doi:10.1038/nature10739

Nonlinear material behaviour of spider silk yields robust webs

Steven W. Cranford[1,2], Anna Tarakanova[1,2,3], Nicola M. Pugno[4] & Markus J. Buehler[1,2,5]

Natural materials are renowned for exquisite designs that optimize function, as illustrated by the elasticity of blood vessels, the toughness of bone and the protection offered by nacre[1–5]. Particularly intriguing are spider silks, with studies having explored properties ranging from their protein sequence[6] to the geometry of a web[7]. This material system[8], highly adapted to meet a spider's many needs, has superior mechanical properties[9–15]. In spite of much research into the molecular design underpinning the outstanding performance of silk fibres[1,6,10,13,16,17], and into the mechanical characteristics of web-like structures[18–21], it remains unknown how the mechanical characteristics of spider silk contribute to the integrity and performance of a spider web. Here we report web deformation experiments and simulations that identify the nonlinear response of silk threads to stress—involving softening at a yield point and substantial stiffening at large strain until failure—as being crucial to localize load-induced deformation and resulting in mechanically robust spider webs. Control simulations confirmed that a nonlinear stress response results in superior resistance to structural defects in the web compared to linear elastic or elastic–plastic (softening) material behaviour. We also show that under distributed loads, such as those exerted by wind, the stiff behaviour of silk under small deformation, before the yield point, is essential in maintaining the web's structural integrity. The superior performance of silk in webs is therefore not due merely to its exceptional ultimate strength and strain, but arises from the nonlinear response of silk threads to strain and their geometrical arrangement in a web.

Although spider silk is used by spiders for many purposes, from wrapping prey to lining retreats[22,23], here we focus on silk's structural role in aerial webs and on how silk's material properties relate to web function. The mechanical behaviour of silk, like that of other biological materials, is determined by the nature of its constituent molecules and their hierarchical assembly into fibres[13,16,17,24–26] (Supplementary Fig. 1). Spider webs themselves are characterized by a highly organized geometry that optimizes their function[7,8,18–20]. To explore the contribution of the material characteristics to web function, we developed a web model with spiral and radial threads based on the geometry commonly found in orb webs[1]. The silk material behaviour was parameterized from atomistic simulations of dragline silk from the species *Nephila clavipes* (model A)[16,17] (Fig. 1a, b) and validated against experiments[10] (Methods Summary). Properties of silk can vary across evolutionary lineages by over 100% (refs 9, 27 and 28; Supplementary Information section 1), so we avoided species-specific silk properties and instead used a representative model to reflect the characteristic nonlinear stress–strain (σ–ε) behaviour of silk found in a web. The mechanical performance of individual silk threads has been previously investigated[10,12,13], and is in agreement with our model in terms of tensile deformation behaviour.

It is rare to see a perfectly intact web—debris, attack or unstable anchorage lead to loss of threads (see inset to Fig. 1c)—but the structure usually remains functional for a spider's use. We assessed a web's ability to tolerate defects by removing web sections (silk threads) and applying a local load (Fig. 1c). Removal of up to 10% of threads, at different locations relative to the load, had little impact on the web's response; in fact, the ultimate load capacity increased by 3–10% with the introduction of defects (Fig. 1c). We observed in all cases that failure is limited to the thread to which the force is applied. Loading of a spiral thread resulted in relatively isolated web distortion (Fig. 1e), whereas loading of a radial thread (Fig. 1f) resulted in larger deformation (about 20% more deflection and about 190% increase in energy dissipation; Fig. 1d). But in both cases, failure was localized (Fig. 1e, f). A comparative study of loading radial versus spiral threads demonstrated that the web's structural performance is dominated by the properties of the stiffer and stronger radial dragline silk (with the force required to break radial threads within the web approximately 150% higher), suggesting that the spiral threads play non-structural roles (such as capturing prey).

In situ experiments on a garden spider (*Araneus diadematus*) web (Fig. 1e, f) were in qualitative agreement with the simulations: they confirmed the prediction that failure is localized when loading either a spiral or a radial thread. Complementing these findings, we used our atomistic silk model[16,17] to connect the stress states in the web (Fig. 2a, top row) with molecular deformation mechanisms in the threads (Fig. 1a). Under loading and immediately before failure, most radial threads in the structure exhibited deformation states equivalent to the yield regime (regime II in Fig. 1a), where the presence of polymer-like semi-amorphous regions permits entropic unfolding of the silk nanocomposite under relatively low stress[16,17,29]. Once unfolding is complete, the system stiffens as stress is transferred to relatively rigid β-sheet nanocrystals[17] (regimes III–IV in Fig. 1a); it finally fails, at the thread where force is applied, because the applied stress is sufficient to rupture the nanocrystals.

Simulation and experiment both indicated that localized failure is a universal characteristic of spider webs. It is unresolved whether this behaviour is unique to silk-like materials or a result of the web's architecture (that is, a property of the construction material or of the structural design). We therefore systematically compared the response of webs constructed from three different types of fibres with distinct mechanical behaviour (Fig. 2a, left panels): in addition to fibres with the atomistically derived stress–strain behaviour of dragline silk (model A), we used idealized engineered fibres that exhibited either linear elastic behaviour (model A′) or elastic–perfectly plastic behaviour that involves severe softening (plastic yield) (model A′′). In all cases, we loaded one of the radial threads and assumed that the failure stress (about 1,400 MPa) and strain (about 67%) of silk threads are constant, so that any changes in deformation behaviour (Fig. 2a, right

[1]Laboratory for Atomistic and Molecular Mechanics (LAMM), Department of Civil and Environmental Engineering, Massachusetts Institute of Technology, 77 Massachusetts Avenue, Cambridge, Massachusetts 02139, USA. [2]Center for Materials Science and Engineering, Massachusetts Institute of Technology, 77 Massachusetts Avenue, Cambridge, Massachusetts 02139, USA. [3]Department of Applied and Engineering Physics, Cornell University, Ithaca, New York 14853, USA. [4]Laboratory of Bio-Inspired Nanomechanics "Giuseppe Maria Pugno", Department of Structural Engineering and Geotechnics, Politecnico di Torino, Corso Duca degli Abruzzi 24, 10129 Torino, Italy. [5]Center for Computational Engineering, Massachusetts Institute of Technology, 77 Massachusetts Avenue, Cambridge, Massachusetts 02139, USA.

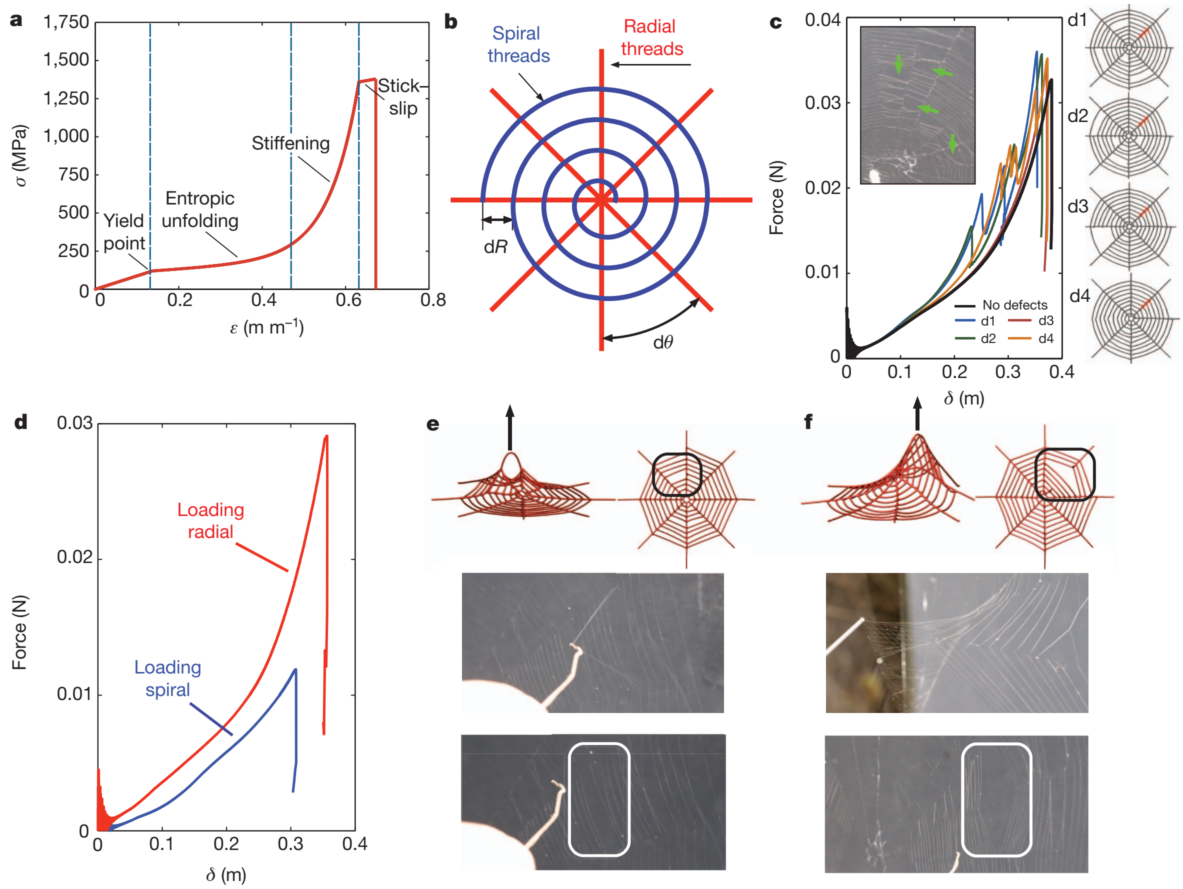

Figure 1 | Material behaviour of dragline spider silk, web model, and behaviour of webs under load. a, Derived stress–strain (σ–ε) behaviour of dragline silk, parameterized from atomistic simulations and validated against experiments[16,17]. There are four distinct regimes characteristic of silk[16,17]. I, stiff initial response governed by homogeneous stretching; II, entropic unfolding of semi-amorphous protein domains; III, stiffening regime as molecules align and load is transferred to the β-sheet crystals; and IV, stick–slip deformation of β-sheet crystals[16] until failure. **b**, Schematic of web model, approximated by a continuous spiral (defined by dR) supported by eight regular radial silk threads (defined by dθ), typical of orb webs[7]. **c**, Force–displacement curves for loading a defective web (results for model A; loaded region shown in red). Case studies include missing spiral segments (d1 to d3) and a missing radial thread (d4). The inset to **c** shows the *in situ* orb web as discovered, containing many defects (marked by green arrows). **d**, Force–displacement behaviour of web, comparing the loading of a single radial thread and a single spiral thread (model A). **e**, Loading of a spiral thread results in small web deformation. **f**, Loading applied at radial threads results in an increase in web deformation. In both cases (**e** and **f**) failure is isolated to the pulled thread in simulation and experiment, restricting damage to a small section of the web (indicated by white rectangles).

panels) and web damage (Fig. 2a, middle panels) would be a direct result of differences in the stress–strain behaviour of the fibres. In the case of a web comprised of natural dragline silk (top panels of Fig. 2a), all radial threads contributed partially to the resistance to loading, but the fact that the material suddenly softened at the yield point, which immediately reduced the initial modulus (about 1,000 MPa) by around 80%, ensured that only the loaded radial thread entered regime III and began to stiffen before it finally failed. With linear elastic material behaviour (middle panels of Fig. 2a), the loaded radial thread was still subjected to the bulk of the load; but adjacent radial threads bore a higher fraction of the ultimate load, which resulted in a greater delocalization of damage upon failure. With elastic–perfectly plastic behaviour (bottom panels of Fig. 2a), the softening of radial threads enhanced the load distribution even more throughout the web and thereby greatly increased the damage zone once failure occurred. The increased contribution of the auxiliary radial threads to load resistance as we moved from the natural to linear elastic to elastic–perfectly plastic behaviour resulted in 34% higher maximum strength, but 30% less displacement at failure (Fig. 2b).

The above simulations using atomistically derived silk properties (model A) assume that the spiral threads and radial threads are made of dragline silk and behave identically, except for differences arising from their different thread diameters. But in real spider webs, spiral threads are composed of more compliant and extensible viscid silk (for example, a failure strain of around 270% for the species *Araneus diadematus*[1]). To explore the effect of different silks making up the spiral and radial threads, we introduced empirically parameterized viscid spiral threads[1] (model B) and found that the results were only marginally affected (Fig. 2b). We also used a model in which we parameterized both spiral and radial threads according to empirical data[1] (model C), subjected this model to the same loading conditions and systematically compared its performance against that of models with linear elastic (model C′) and elastic–perfectly plastic behaviours (model C′′). We found similar web responses and although the web made from natural silk is weaker, it still localizes damage near the loaded region (Supplementary Information section 5).

To explore global loading responses, we subjected the web models to a homogeneously distributed wind load with effective wind speeds up to 70 m s^{-1} (a threshold at which all models fail). The system-level deflection curves (Fig. 2c) reflect the mechanical behaviour of the radial threads, which ultimately transferred load to the web's anchoring points. Although the spiral threads underwent increased deflection and captured more of the wind load owing to their larger exposed length, they were effectively pinned to the much stiffer dragline radial threads that limit web deflection (Fig. 2c, Supplementary Information section 8). For wind speeds less than 10 m s^{-1} there was little difference between the models (Fig. 2c, Supplementary Information section 8) and deflections are <12% of the total span of the web. We attributed

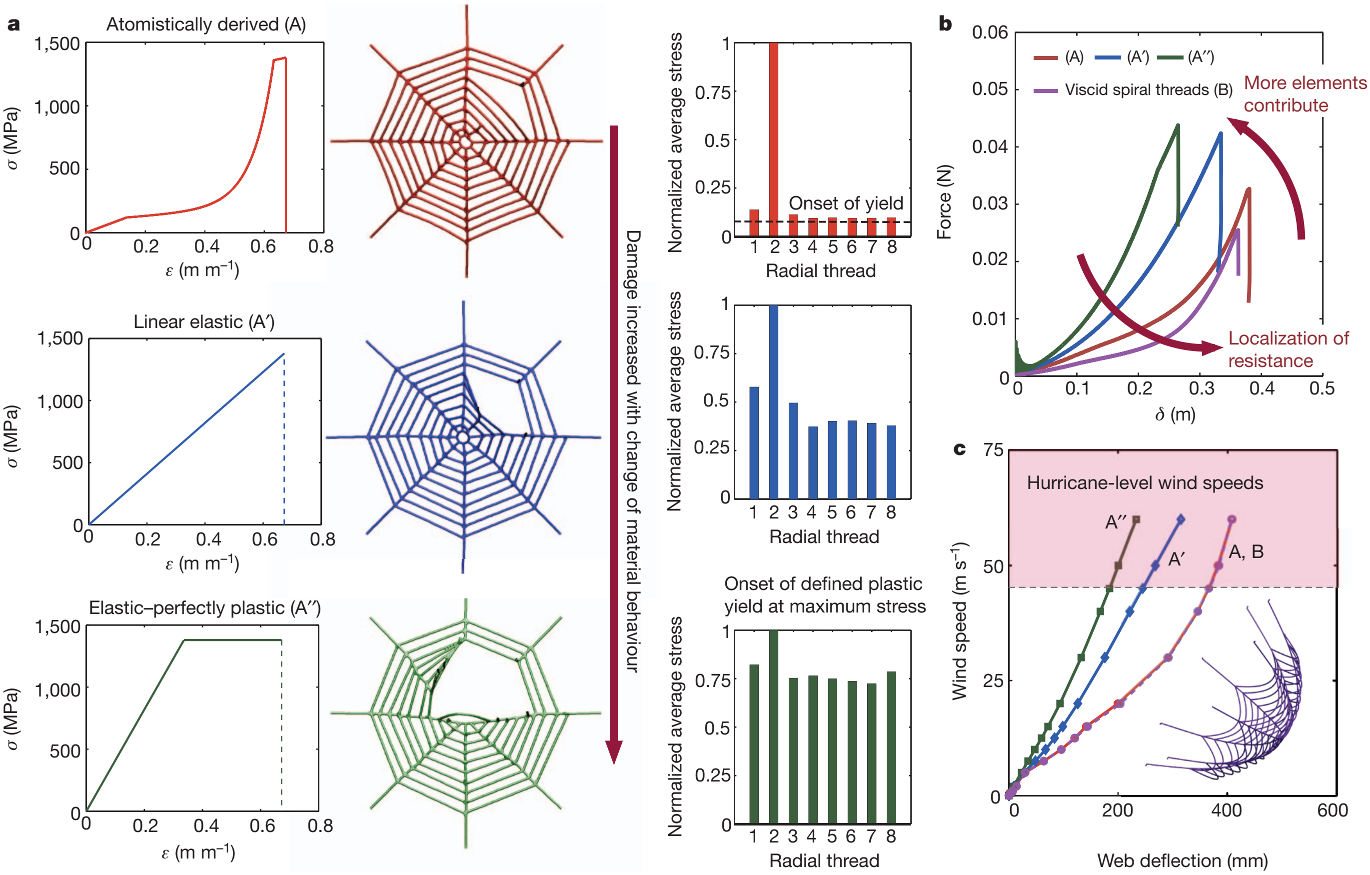

Figure 2 | Web response for varied silk behaviour under targeted (local) and distributed (global) loading. **a**, Comparison of failure for derived dragline silk, linear elastic and elastic–perfectly plastic behaviours (left, models A, A′ and A′′). Comparison of failure (centre) confirms localized stresses and minimized damage for the natural nonlinear stiffening silk behaviour. The average stress of each radial thread (bar plots, right) reflects the nonlinear deformation states in the silk. When load is applied locally to a radial thread, other radial threads not subject to applied force reach a stress corresponding to the onset of yielding (that is, regime II in Fig. 1a). The elastic–perfectly plastic behaviour leads to an almost homogeneous distribution of stress. **b**, Force–displacement curves for varying material behaviours (models A, A′ and A′′ and model B). **c**, Web behaviour under distributed (global) wind loading. The plot shows a comparison of the wind-deflection behaviour (models A, A′, A′′ and B). The initial high stiffness of natural dragline silk enhances the structural integrity of the web under such loading. Failure of all webs occurs at wind speeds in excess of 60 m s^{-1}.

this relatively uniform structural rigidity of the web to the initial stiffness of the dragline silk before yield (Fig. 1a). Under higher wind loads, the softening behaviour of dragline silk at moderate deformation resulted in significant web deflection that was greater than the deflections seen with linear elastic and elastic–perfectly plastic material behaviour (Fig. 2c). We found that yield in the threads occurred at wind speeds exceeding around 5 m s^{-1}, defining a reasonable wind speed regime in which webs are operational.

Although all web models performed similarly under moderate global (wind) loading (Fig. 2c), the linear elastic and elastic–perfectly plastic models responded to targeted force application with a more catastrophic, brittle-like failure that resulted in significantly increased damage. Defining web damage as percentage of failed (broken) threads, we found that the damage of 2.5% for the natural silk behaviour increases sixfold to 15% for the elastic–perfectly plastic model (Fig. 2a, centre panel). Web performance under local loading was generalized by invoking quantized fracture mechanics[30], a theory that describes the failure mechanisms of discrete structures (such as a spider web) and adapted here to incorporate the material behaviours (Supplementary Information section 10). A generalized stress–strain behaviour, where $\sigma \propto \varepsilon^{\kappa}$ (κ is a parameter that defines the nonlinear nature of the stress–strain relationship) treated with quantized fracture mechanics revealed that the size of the damaged zone in the proximity to a defect increases for materials that feature a softening behaviour (elastic–perfectly plastic behaviour), whereas a stiffening material (natural silk) results in a decrease of the damage zone (Fig. 3). This is captured by a scaling law $\Omega(\alpha) = 1 - S^{2\alpha}$, defining the structural robustness Ω as the undamaged fraction of the web after failure. Here $\alpha = \kappa/(\kappa + 1)$ reflects the stress–strain response (linear elastic case when $\alpha = 1/2$; stiffening when α tends to 1 and softening when α tends to 0), and S is a system-dependent constant (independent of stress–strain relation). Our simulation results agreed with the predictions of quantized fracture mechanics (Supplementary Table 5) and confirmed that the relative size of the damage zone is a function of the material stress–strain relation and enhanced by the discreteness of the web (Supplementary Information section 10). This phenomenon is exemplified in spider webs (Figs 1 and 2), where the nonlinear stiffening behaviour (as α tends to 1) is essential for localizing damage and ensuring that a loaded thread becomes a sacrificial element while the majority of the web remains intact. Given the presumed metabolic effort required by the spider for rebuilding an entire web, localized failure is preferential as it does not compromise the structural integrity of the web (see Fig. 1c) and hence allows it to continue to function for prey capture in spite of the damage.

The remarkable strength, toughness and extensibility of individual spider silk threads are thus not the dominating properties that underpin the excellent structural performance of a spider web. Rather, it is the distinct nonlinear softening and subsequent stiffening of dragline silk that is essential to function, as it results in localization of damage to sacrificial threads in a web subjected to targeted (local) loading while minimizing web deformations under moderate wind (global) loading. Each regime of the nonlinear material behaviour of silk (Fig. 1a) thus

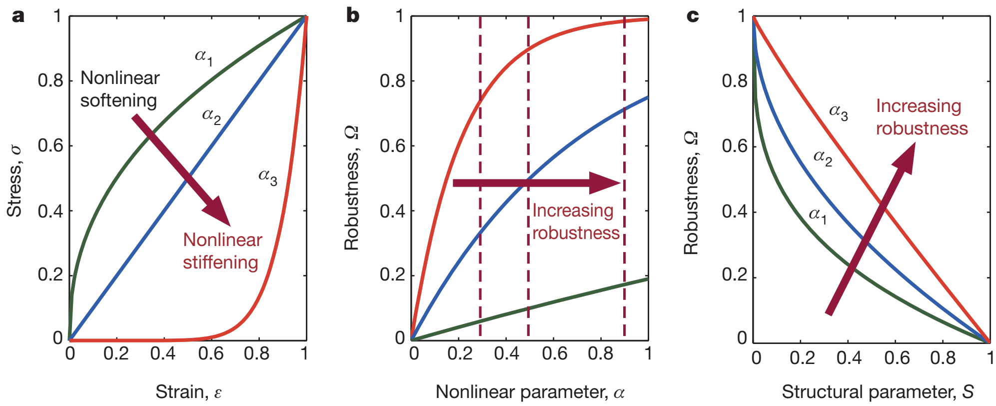

Figure 3 | Effects of stress–strain behaviour on structural robustness via quantized fracture mechanics. **a**, Plots of stress–strain curves (material behaviour) demonstrating the transition from softening to stiffening behaviours by the nonlinear parameter α ($\alpha_1 = 0.3$, $\alpha_2 = 0.5$, $\alpha_3 = 0.9$). **b**, Structural robustness Ω, defined as the undamaged fraction of the structure, versus α (dashed lines indicating α_1, α_2, α_3), given for three values of the system-dependent constant S ($S_1 = 0.1$, $S_2 = 0.5$, $S_3 = 0.9$). S captures a range of material properties (such as fracture toughness), system geometry (that is, crack width or element length), and applied loading conditions. **c**, Ω versus S. Universally, the robustness increases with an increase in α ($\alpha_1 < \alpha_2 < \alpha_3$), implying that larger nonlinear stiffening results in larger structural robustness, and hence less damage.

plays a key part in defining the overall system response in a variety of environmental settings. Other natural silk threads used to form solid materials such as cocoons, rather than aerial webs, typically display different mechanical responses[11]. Indeed, cocoon silk conforms closely to elastic–perfectly plastic behaviour, which is not suitable for web construction. The softening behaviour typically seen in such silks, combined with a solid material structure rather than a discrete mesh, results in a greater spreading of damage that effectively enhances the system's fracture toughness. This is clearly an advantage for the protective role of cocoons, and is reminiscent of other biomaterials where mechanical robustness has been attributed to the formation of large plastic regions[2,5]. The opposite is true for webs, where robustness arises from extreme localization of failure at sacrificial elements, with this behaviour enhanced by the stiffening of threads (Figs 1a and 2a).

The enhanced mechanical performance of the web relies on the integration of material and structure, which ultimately derives from the particular molecular structure of silk that features a composite of semi-amorphous protein and β-sheet nanocrystals. We suggest that web design principles might be considered in engineering, where current practice uses sacrificial elements solely to dissipate energy (for example, impact loading, seismic response). In spider webs, discrete sacrificial elements are instead a means to avoid potentially dangerous system-level loading and mitigate structural damage so that despite the small decrease in spider-web load capacity (Fig. 2b), the robustness of the structure overall is greatly enhanced (Fig. 3). This allows a spider to repair rather than rebuild completely, should failure occur. Such an engineering design could ignore the requirements for the magnitude of a potential load and allow local failure to occur, a design stipulation that requires the consideration of both material behaviour and structural architecture.

METHODS SUMMARY

The web consists of an arithmetic spiral[7] supported by radial threads at regular intervals, constructed from two primary elements, radial threads and spiral threads[7] (Fig. 1b), and is modelled using molecular dynamics procedures. We implement five material behaviours: (1) atomistically derived dragline silk behaviour (parameterized from molecular simulations of dragline silk[16,17]) (Fig. 1a); (2) empirically parameterized dragline silk (from experimental data[1]); (3) empirically parameterized viscid silk (from experimental data[1]); (4) ideal linear elastic behaviour; (5) ideal elastic–perfectly plastic behaviour, incorporated in three arrangements in models A, B and C. We consider two types of application of loading, targeted (local) and global (wind) loading. To characterize the mechanical response of the web under targeted loading, a spring-load is imposed to a small section of the web and increased until failure is incurred (defined by the failure of loaded threads). Wind loading is applied via a constant drag force applied to all web threads. *In situ* experiments through simple mechanical assays are applied to an orb web of the common European garden spider. We identify a web in its natural environment and deform radial and spiral threads using a mechanical applicator (a metal wire to load threads). During deformation we control the displacement and monitor images using a digital camera. For theoretical analysis we use quantized fracture mechanics[30], a theory that describes the failure of discrete structures such as a spider web and adapted here to incorporate the nonlinear stress–strain behaviour of silk. For a detailed description of the models see Methods and Supplementary Information.

Full Methods and any associated references are available in the online version of the paper at www.nature.com/nature.

Received 22 November 2010; accepted 25 November 2011.

1. Gosline, J. M., Guerette, P. A., Ortlepp, C. S. & Savage, K. N. The mechanical design of spider silks: from fibroin sequence to mechanical function. *J. Exp. Biol.* **202,** 3295–3303 (1999).
2. Gao, H., Ji, B., Jäger, I. L., Arzt, E. & Fratzl, P. Materials become insensitive to flaws at nanoscale: lessons from nature. *Proc. Natl Acad. Sci. USA* **100,** 5597–5600 (2003).
3. Aizenberg, J. *et al.* Skeleton of *Euplectella* sp.: structural hierarchy from the nanoscale to the macroscale. *Science* **309,** 275–278 (2005).
4. Vollrath, F. Spider webs and silks. *Sci. Am.* **266,** 70–76 (1992).
5. Kamat, S., Su, X., Ballarini, R. & Heuer, A. H. Structural basis for the fracture toughness of the shell of the conch *Strombus gigas*. *Nature* **405,** 1036–1040 (2000).
6. Lefèvre, T., Rousseau, M. E. & Pézolet, M. Protein secondary structure and orientation in silk as revealed by Raman spectromicroscopy. *Biophys. J.* **92,** 2885–2895 (2007).
7. Vollrath, F. & Mohren, W. Spiral geometry in the garden spider's orb web. *Naturwissenschaften* **72,** 666–667 (1985).
8. Vollrath, F. Silk evolution untangled. *Nature* **466,** 319 (2010).
9. Agnarsson, I., Kuntner, M. & Blackledge, T. A. Bioprospecting finds the toughest biological material: extraordinary silk from a giant riverine orb spider. *PLoS ONE* **5,** e11234 (2010).
10. Du, N. *et al.* Design of superior spider silk: from nanostructure to mechanical properties. *Biophys. J.* **91,** 4528–4535 (2006).
11. Shao, Z. Z. & Vollrath, F. Materials: surprising strength of silkworm silk. *Nature* **418,** 741 (2002).
12. Omenetto, F. G. & Kaplan, D. L. New opportunities for an ancient material. *Science* **329,** 528–531 (2010).
13. Ko, K. K. *et al.* Engineering properties of spider silk. *Adv. Fibers Plastics Laminates Composites* **702,** 17–23 (2002).
14. Rammensee, S., Slotta, U., Scheibel, T. & Bausch, A. R. Assembly mechanism of recombinant spider silk proteins. *Proc. Natl Acad. Sci. USA* **105,** 6590–6595 (2008).
15. Vollrath, F., Holtet, T., Thogersen, H. C. & Frische, S. Structural organization of spider silk. *Proc. R. Soc. Lond. B* **263,** 147–151 (1996).
16. Keten, S., Xu, Z. P., Ihle, B. & Buehler, M. J. Nanoconfinement controls stiffness, strength and mechanical toughness of beta-sheet crystals in silk. *Nature Mater.* **9,** 359–367 (2010).
17. Keten, S. & Buehler, M. J. Nanostructure and molecular mechanics of spider dragline silk protein assemblies. *J. R. Soc. Interf.* **7,** 1709–1721 (2010).
18. Aoyanagi, Y. & Okumura, K. Simple model for the mechanics of spider webs. *Phys. Rev. Lett.* **104,** 038102 (2010).
19. Ko, F. K. & Jovicic, J. Modeling of mechanical properties and structural design of spider web. *Biomacromolecules* **5,** 780–785 (2004).

20. Alam, M. S., Wahab, M. A. & Jenkins, C. H. Mechanics in naturally compliant structures. *Mech. Mater.* **39,** 145–160 (2007).
21. Alam, M. S. & Jenkins, C. H. Damage tolerance in naturally compliant structures. *Int. J. Damage Mech.* **14,** 365–384 (2005).
22. Foelix, R. F. *Biology of Spiders* 2nd edn (Oxford University Press/Georg Thieme, 1996).
23. Vollrath, F. Biology of spider silk. *Int. J. Biol. Macromol.* **24,** 81–88 (1999).
24. Termonia, Y. Molecular modeling of spider silk elasticity. *Macromolecules* **27,** 7378–7381 (1994).
25. Vepari, C. & Kaplan, D. L. Silk as a biomaterial. *Prog. Polym. Sci.* **32,** 991–1007 (2007).
26. Swanson, B. O., Blackledge, T. A. & Hayash, C. Y. Spider capture silk: performance implications of variation in an exceptional biomaterial. *J. Exp. Zool. A* **307A,** 654–666 (2007).
27. Swanson, B. O., Anderson, S. P., DiGiovine, C., Ross, R. N. & Dorsey, J. P. The evolution of complex biomaterial performance: the case of spider silk. *Integr. Comp. Biol.* **49,** 21–31 (2009).
28. Vollrath, F. & Selden, P. The role of behavior in the evolution of spiders, silks, and webs. *Annu. Rev. Ecol. Evol. Syst.* **38,** 819–846 (2007).
29. Keten, S. & Buehler, M. J. Atomistic model of the spider silk nanostructure. *Appl. Phys. Lett.* **96,** 153701 (2010).
30. Pugno, N. M. & Ruoff, R. S. Quantized fracture mechanics. *Phil. Mag.* **84,** 2829–2845 (2004).

Supplementary Information is linked to the online version of the paper at www.nature.com/nature.

Acknowledgements This work was supported primarily by the Office of Naval Research (N000141010562) with additional support from the National Science Foundation (MRSEC DMR-0819762, the NSF-REU programme, as well as CMMI-0642545) and the Army Research Office (W911NF-09-1-0541 and W911NF-10-1-0127). Support from the MIT-Italy programme (MITOR) and a Robert A. Brown Presidential Fellowship is gratefully acknowledged. N.M.P. is supported by the METREGEN grant (2009-2012) ''Metrology on a cellular and macromolecular scale for regenerative medicine''. An Ideas Starting Grant 2011 BIHSNAM on ''Bio-inspired hierarchical super nanomaterials'' was awarded to N.M.P. from the European Research Council, under the European Union's Seventh Framework Programme (FP7/2007-2013)/ERC grant (agreement number 279985). All simulations have been carried out at MIT's Laboratory for Atomistic and Molecular Mechanics (LAMM). We acknowledge assistance from S. and E. Buehler in taking photographs of the spider web.

Author Contributions S.W.C. and M.J.B. designed the research and analysed the results. S.W.C. and A.T. developed the material models, performed the simulations, and conducted the simulation data analysis. M.J.B. performed the *in situ* experiments and analysed the results. N.M.P. contributed the theoretical analysis and predictions and analysed the results. S.W.C., M.J.B., A.T. and N.M.P. wrote the paper.

Author Information Reprints and permissions information is available at www.nature.com/reprints. The authors declare no competing financial interests. Readers are welcome to comment on the online version of this article at www.nature.com/nature. Correspondence and requests for materials should be addressed to M.J.B. (mbuehler@mit.edu).

METHODS

Web geometry. Previous web models have implemented simplified versions of web geometry, most commonly in a concentric circle arrangement[18–20]. Here we modelled a realistic orb web and approximated it by an arithmetic spiral[7] defined by the polar equation $R(\theta) = \alpha \times \theta$, where spiral spacing is defined by $dR = 2\pi\alpha$, supported by radial threads at regular angular intervals ($d\theta = 45^{\circ}$). The basic web structure was constructed from two primary silk elements—radial threads and spiral threads[7]—combined with glue-like connections (Fig. 1b). The web was formed by particle-spring elements, with an equilibrium spacing of $r_0 = 0.01$ m. In nature, the construction of a stereotypical orb web includes the placement of framing threads that act as mooring and a structural foundation for the web[7]. The arrangement of such threads varies according to the anchoring points available to the spider and clearly has the strength necessary to bear the interior web, so we neglect it here. For a detailed description of the model, see Supplementary Information section 2.

Web models. We used web models based on combinations of five material behaviours: (1) atomistically derived dragline silk (parameterized from molecular simulations of dragline spider silk[16,17]) (Fig. 1a); (2) empirically parameterized dragline silk (from experimental data[1]); (3) empirically parameterized viscid silk (from experimental data[1]); (4) ideal linear elastic behaviour; and (5) ideal elastic–perfectly plastic behaviour. To explore the differences between the theoretically derived silk models with experimentally measured silks, the materials were implemented in the following three web models.

Model A. We used atomistically derived dragline silk behaviour for both the radial and spiral threads (details in Supplementary Information section 3.1), to maintain independence from empirical data. Even though such a simple model formulation did not allow us to draw conclusions about phenomena pertaining to specific types of silk, it did enable us to understand universal, generic relationships between underlying molecular mechanisms, the resulting nonlinear properties of the material, and the failure behaviour of webs. The dragline radial behaviour was used for fitting corresponding linear elastic (model A′, see Supplementary Information section 3.3) and elastic–perfectly plastic (model A′′, see Supplementary Information section 3.4) models, as indicated in Fig. 2a.

Model B. We combined atomistically derived dragline silk for radial threads (see Supplementary Information section 3.1) with empirically parameterized viscid silk behaviour for spiral threads (see Supplementary Information section 3.2), to examine the effect of deviations in the stiffness of viscid silk (naturally more compliant than dragline silk). Because idealized behaviours (linear elastic or elastic–perfectly plastic) are parameterized on the basis of the radial response, there are no idealized iterations of model B.

Model C. This was a completely empirically parameterized web model, with empirically fitted dragline silk for the radial threads (described in Supplementary Information section 3.2) and empirically fitted viscid silk for spiral threads, for a realistic web representation tuned by experimental data[1]. The empirical dragline behaviour is for fitting corresponding linear elastic (model C′, see Supplementary Information section 3.3) and elastic–perfectly plastic behaviour (model C′′, see Supplementary Information section 3.4).

The results of the empirically parameterized model are discussed in Supplementary Information section 5. The model framework used here can easily be adapted for other species of spiders, associated silk properties, and web geometries. Using a particle dynamics formulation (motivated by molecular dynamics), the total energy of the web system was defined as:

$$U_{\mathrm{web}} = \Sigma_{\mathrm{threads}}\phi_{\mathrm{material}} \tag{1}$$

for the summation of the elastic potentials of all the silk threads, where ϕ_{material} refers to the constitutive energy expression of the specific material.

Atomistically derived dragline silk. To parameterize silk deformation behaviour, we use data from previous full atomistic simulations of major ampullate dragline spider silk[16,17,32,33], unaccounted for in previous web studies[18–20]. The constitutive behaviour of dragline silk was formulated as:

$$\varphi_{\mathrm{dragline}}(r) = A_0 \times \begin{cases} \frac{1}{2}\frac{E_1}{r_0}(r - r_0)^2, \ r \le r_y \\ \frac{r_0}{\alpha}\exp\left[\frac{\alpha(r - r_y)}{r_0}\right] + \frac{1}{2}\frac{\beta}{r_0}(r - r_y)^2 + C_1(r - r_y) + C_3, \ r_y \le r < r_s \\ \frac{1}{2}\frac{E_2}{r_0}(r - r_s)^2 + C_2(r - r_s) + C_4, \ r_s \le r < r_b \\ 0, \ r \ge r_b \end{cases} \tag{2}$$

See Supplementary Table 1 for all parameters.

Empirically parameterized silk. To assess the generality of the results obtained with our atomistically derived behaviour, we implemented empirically fitted material behaviours for models B and C[1]. The functional form of the empirically parameterized dragline (radial) silk was identical to that of the atomistically derived dragline silk (described by equation (2)). To represent the J-shaped viscid silk response measured in experimental studies, we used a combined linear and exponential function:

$$\varphi_{\mathrm{viscid}}(r) = A_0 \times \left(ar_0 \exp\left(\frac{r - r_0}{r}\right) + \frac{1}{2}br\frac{(r - 2r_0)}{r} + cr\right) \quad \text{for} \quad r < r_b \tag{3}$$

We fitted the parameters in equations (2) and (3) to experiments on *Araneus diadematus*[1] for both dragline and viscid silk. See Supplementary Table 2 for all parameters.

Idealized material behaviours. For comparison, motivated by earlier studies[31], we implemented a model that allowed us systematically to vary the nature of nonlinear behaviour, permitting cases of ideal linear elastic and ideal elastic–perfectly plastic (softening) behaviour, to develop general insight. The linear elastic behaviour was governed by:

$$\varphi_{\mathrm{linear}}(r) = \frac{1}{2}\left(\frac{E_{\mathrm{linear}}A_0}{r_0}\right)(r - r_0)^2 \quad \text{for} \quad r < r_b \tag{4}$$

while the elastic–perfectly plastic behaviour was governed by:

$$\varphi_{\mathrm{plastic}}(r) = \begin{cases} \frac{E_{\mathrm{plastic}}A_0}{2r_0}(r - r_0)^2, \ r_0 \le r < r_y \\ \frac{E_{\mathrm{plastic}}A_0}{2r_0}(r_y - r_0)^2 + \frac{E_{\mathrm{plastic}}A_0}{r_0}(r_y - r_0)(r - r_y), \ r_y \le r < r_b \end{cases} \tag{5}$$

Both behaviours were parameterized to reflect either the ultimate stress and strain of atomistically derived dragline silk (in model A) or the ultimate stress and strain of empirically parameterized dragline silk (in model C) to provide a comparison between material laws and web performance. See Supplementary Tables 3 and 4 for all parameters.

Loading conditions. We considered two types of loading, targeted (local) and global (wind) loading. To characterize the mechanical response and robustness of the web under local load, a load was imposed on a small section of the web (see Supplementary Information section 4), representing, for example, a small piece of debris. The spring-load is increased until failure occurred (defined by the failure of all loaded threads). Load was imposed on a small section of the web in the out-of-plane direction, offset from the centre of the web. Proximity to the web centre maximizes the structural resistance of the entire web (as compared to loading the web periphery, for example), while the offset is used to apply the load to a known (chosen) radial thread to ease analysis. We determined the deflection of the web (out-of-plane) and applied force. We calculated the work needed to break individual threads by numerically integrating the force–displacement curves (see Supplementary Information section 6). To characterize the mechanical response under wind load (global), we applied a constant force to the entire web structure, derived from the equivalent drag force on a cylindrical wire (see Supplementary Information section 8). Loads for equivalent wind speeds of 0.5 to 70 m s^{-1} are applied (all models fail at 70 m s^{-1} winds).

***In situ* experimental studies.** We carried out experiments on a physical web on the basis of mechanical assays applied to an orb web of the common European garden spider discovered in southern Germany. We identified a large spider web in its natural environment and ensured that the spider web was in use by a living spider. We deformed radial and spiral threads using a mechanical applicator, a small piece of wire that can effectively be used to pull on small structural features. During mechanical deformation of the web we controlled the displacement and monitored visual images of the web using a digital camera (results shown in Fig. 1e, f). A black plastic plate was placed behind the web to ensure that the web was clearly visible during the experiment for image acquisition.

Stress distribution. Normalized strain energy distributions were considered for radial threads just before and immediately after web fracture to calculate the average stress according to equations (2) to (5) (normalized with respect to maximum strain energy at ultimate failure). Spiral threads were not considered because most of the load (and thus elastic resistance) is carried by the radials in this load interval (see Supplementary Information section 9).

Theoretical analysis. We used quantized fracture mechanics[30], adapted here to incorporate the nonlinear material behaviour of silk using a generalized stress–strain (σ–ε) behaviour of $\sigma \propto \varepsilon^{\kappa}$. The relative size of the damage zone after failure was given by:

$$\varphi(\alpha) = S^{2\alpha} \tag{6}$$

where S is a system-dependent constant reflective of specific material properties (such as fracture toughness), system geometry, and applied loading conditions.

The constant S describes the damage associated with the linear elastic behaviour when 2α tends to 1 and therefore $\varphi = S$. The fraction of surviving material after failure defines structural robustness:

$$\Omega(\alpha) = 1 - S^{2\alpha} \tag{7}$$

The parameter S was determined from the linear elastic response as the reference case, and constant for all variations in the stress–strain behaviour. The three material behaviours studied here (Fig. 2a), characteristic of silk, linear elastic and elastic–perfectly plastic behaviours, were reduced to general nonlinear stress–strain power laws fitted by a single nonlinearity parameter α in the quantized fracture mechanics theory (Fig. 3). For details see Supplementary Information section 10.

31. Buehler, M. J. & Gao, H. Dynamical fracture instabilities due to local hyperelasticity at crack tips. *Nature* **439,** 307–310 (2006).
32. Nova, A., Keten, S., Pugno, N. M., Redaelli, A. & Buehler, M. J. Molecular and nanostructural mechanisms of deformation, strength and toughness of spider silk fibrils. *Nano Lett.* **10,** 2626–2634 (2010).
33. van Beek, J. D., Hess, S., Vollrath, F. & Meier, B. H. The molecular structure of spider dragline silk: folding and orientation of the protein backbone. *Proc. Natl Acad. Sci. USA* **99,** 10266–10271 (2002).

doi:10.1038/nature10739

An integrated material/structure understanding in the description of web mechanics as outlined in **Fig. S1** has yet to be implemented and is reported in this paper.

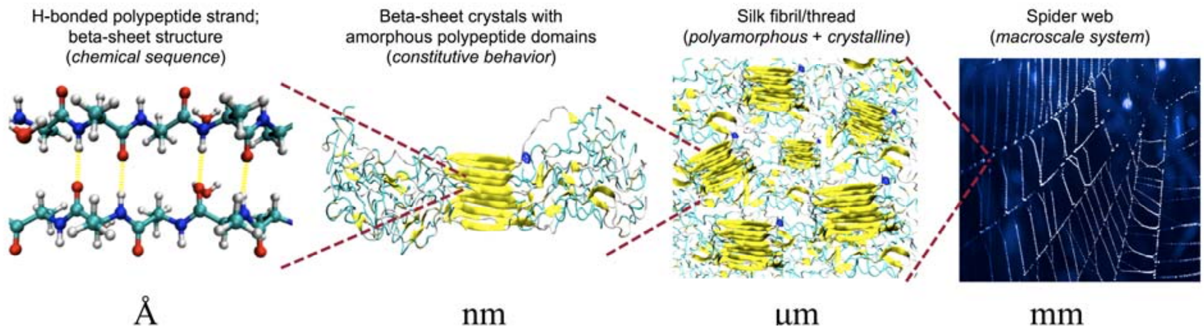

Figure S1 | Schematic of the hierarchical spider silk structure that ranges from nano (Angstrom) to macro (millimetres). The image displays key structural features of silk, including the chemical structure found at the level of polypeptide β-strands, the secondary structure *β*-sheet nanocrystals embedded in a softer semi-amorphous phase, bulk assembly of poly-crystalline components which assemble into macroscopic silk fibres, and finally the web-structure itself

S1. Silk types and variation

The spider web, although a common and recognized biological structure, is an evolutionary product with a myriad of functions, including the capturing of prey[28]. Beyond the web itself, spiders use silk for a number of activities central to their survival and reproduction, including wrapping of egg sacks, preparing safety lines, and lining retreats[22,23]. Even within a web, there are multiple types of silk that serve distinct purposes[4,34]. For instance, dragline silk is produced from the spider's major ampullate (MA) silk glands, with a unique and well researched constitutive behaviour, and important as a structural element in webs[35]. Yet, even though most spiders produce some form of dragline silk, the specific material properties vary among different evolutionary lineages of spiders[27,28,36,37,38]. Even among orb web weaving spiders (in which dragline silk serves a similar purpose) the material properties of dragline silk vary by more than 100%, and across all spiders toughness varies over twenty fold in species examined to date[9]. Another key silk type within the web is the sticky capture silk, made of a viscid silk that originates from flagelliform glands[35,39,40] and used to form the spiral threads in a web. Both viscid and dragline silks express a stiffening stress-strain behaviour, where viscid silk is approximately ten times more extensible than dragline silk[35,39]. Dragline silk is the most well researched silk with theoretical[24], computational[20], and experimental[10] studies across a multitude of scales elucidating its mechanical behaviour. The web itself is intriguing as a natural structure, and has been investigated from a biological, functional, and structural point of view[41]. Of the tremendous diversity of spider web types, the orbicular webs of the araneid orb weaving spiders are the most accessible analytically[4,16,42].

S2. Web model geometry, connectivity, and elements

Here we aim to mimic a realistic web structure and approximate the orb web by an arithmetic spiral[7,42]. The 'spiral' components are defined as an Archimedes' spiral, defined by the polar equation:

$$R(\theta) = \alpha \cdot \theta \tag{S1}$$

The coils of successive turns are spaced in equal distances ($dR = 2\pi\alpha$). For all models generated, $\alpha = 0.005$ m, resulting in $dR \approx 31$ mm. The spiral is defined by prescribing θ in a range from $360° \rightarrow 3600°$. To ensure the inter-particle spacing is approximately the prescribed inter-particle distance, the spiral arc length between consecutive particles is calculated, where:

$$ds = s(\theta_i) - s(\theta_{i-1}) \tag{S2}$$

and

$$s(\theta_i) = \frac{1}{2}\alpha\left[\theta_i\sqrt{1+{\theta_i}^2} + \ln\left(\theta_i + \sqrt{1+{\theta_i}^2}\right)\right]. \tag{S3}$$

A constant increment in angle, $d\theta$, results in a monotonically increasing ds. As such, we implement an iterative loop to reduce $d\theta$ as the spiral radius increases, ensuring that $ds < 1.05r_0$, where r_0 is the initial (chosen), inter-particle spacing (0.01 m). The numerical factor 1.05 is included to provide stochastic variation in structure, representing a more realistic spider web as opposed to a perfect spiral, and also accounts for the slight difference between arc length and chord length between consecutive particle positions. Radial threads are prescribed at regular intervals ($d\theta = 45°$), and span 0.4 m in the radial direction.

In physical webs, the interconnection of the different silks in an orb-web is, however, accomplished via a gluey, silk-like substance termed "attachment cement" originating from the piriform gland of spiders[34,43,44,45]. Here, we account for these discrete or non-continuous radial-spiral connections via the introduction of "attachment bonds" to reflect the attachment cement of physical orb webs. There exist four types of bonds and springs (elements) for connectivity in all web models considered here:

1. **Radial bonds** (representing radial threads); consisting of 40 particles spaced 10 mm apart in the radial direction, connected consecutively.
2. **Inner radial circle connections**, to avoid stress concentration by a common connection point. Each radial thread is connected to a small, inner circle at the centre of the spiral with a radius of 10 mm consisting of 16 particles. The stress-strain behaviour is that of the radial threads.
3. **Spiral bonds** (representing spiral threads) in a continuous spiral, particles spaced ≈10 mm, connected consecutively.
4. **Radial-spiral connections** (representing silk-like "attachment cement"). A scripted algorithm used to connect spiral to radial threads at cross-over regions if the distance between the spiral bead and nearest radial bead is less than 8 mm. Resulted in 1-3 connections per cross-over region. Stress-strain behaviour is that of the radial dragline threads.

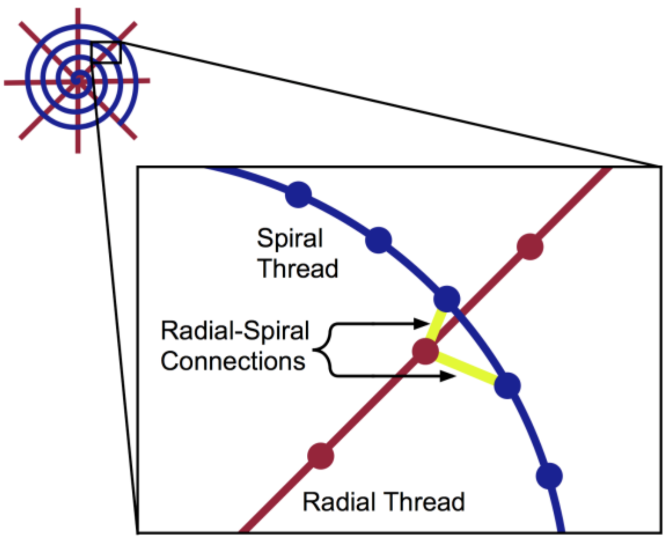

Figure S2 | Schematic of radial-spiral connection configuration. The overlaid spiral silk thread is attached to the radial threads by bonds reflective of attachment cement of physical orb webs. The material behaviour of the connections is equivalent to the radial threads.

S3. Material behaviours

We parameterize and implement five material behaviours:

(i) atomistically derived dragline silk behaviour (see **Section S3.1**);
(ii) empirically parameterized dragline silk (see **Section S3.2**);
(iii) empirically parameterized viscid silk (see **Section S3.2**);
(iv) ideal linear elastic behaviour (see **Section S3.3**);
(v) ideal elastic-perfectly-plastic behaviour (see **Section S3.4**)

Different material combinations are implemented to explore potential differences between the theoretically derived silk behaviours (atomistically derived and parameterized Model A; with variations A', and A") with experimentally measured silks (compliant viscid silk introduced in Model B, and a completely empirically fitted and parameterized Model C; with variations C', and C").

S3.1 Atomistically derived dragline silk

This material behaviour utilizes a combination of linear and exponential functions to determine the stress-strain behaviour of the silk, defined by four parameters reflecting stiffness, and three critical strains.

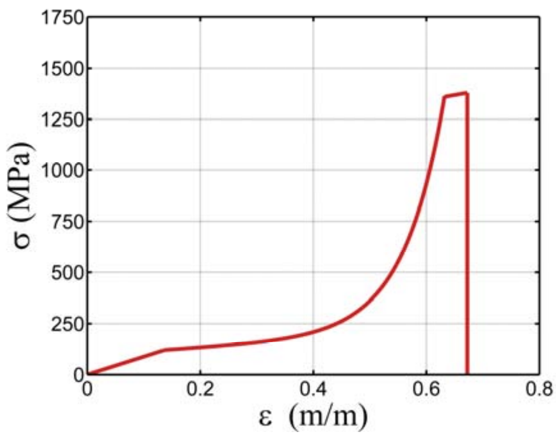

Figure S3 | Stress-strain behaviour implemented for atomistically derived dragline silk (radial and spiral threads of Model A and radial threads of Model B; see Eq. (S4)). The nonlinear behaviour is separated into four regimes: (*i*) linear until yielding; (*ii*) entropic unfolding; (*iii*) exponential stiffening, and; (*vi*) a stick-slip plateau until failure.

The stress-strain function is expressed as:

$$\sigma(\varepsilon)=\begin{cases} E_1\varepsilon & , 0\le\varepsilon<\varepsilon_y \\ \exp\left[\alpha\left(\varepsilon-\varepsilon_y\right)\right]+\beta\left(\varepsilon-\varepsilon_y\right)+C_1 & , \varepsilon_y\le\varepsilon<\varepsilon_s \\ E_2(\varepsilon-\varepsilon_s)+C_2 & , \varepsilon_s\le\varepsilon<\varepsilon_b \\ 0 & , \varepsilon\ge\varepsilon_b \end{cases} \tag{S4}$$

defined by four parameters (E_1, E_2, α, and β) reflecting stiffnesses, and three corresponding critical strains (ε_y, ε_s, ε_b) given in **Table S1**.

Parameter	Value
Initial stiffness, E_1	875.9 MPa
Exponential parameter, α	14.2
Tangent stiffness parameter, β	180 MPa
Final stiffness, E_2	491.2 MPa
Yield strain, ε_y	0.1356
Softening strain, ε_s	0.6322
Ultimate (breaking) strain, ε_b	0.6725
Radial thread diameter (from [18,40])	3.93 μm
Spiral thread diameter (from [18,40])	2.40 μm

Table S1 | Atomistically derived dragline silk stress-strain behaviour parameters (implemented in radial and spiral threads in Model A, radial threads only in Model B). Radial and spiral thread diameters taken from experimental findings[18,40].

The constants C_1 and C_2 ensure continuity, where $C_1 = E_1\varepsilon_y - 1$, and $C_2 = \exp[\alpha(\varepsilon_s - \varepsilon_y)] + \beta(\varepsilon_s - \varepsilon_y) + C_1$. For tensile stretching, the stress-strain behaviour is converted to a force-displacement spring function, to allow a molecular dynamics implementation, given by:

$$F(r) = A_0 \cdot \sigma(\varepsilon(r)), \tag{S5}$$

and $\varepsilon(r) = \frac{r - r_0}{r_0}$, such that $r_y = r_0(1 + \varepsilon_y)$, $r_s = r_0(1 + \varepsilon_s)$, and $r_b = r_0(1 + \varepsilon_b)$. Subsequently, the spring (force-displacement) relation is used to determine the energy between all bonded pairs of particles, with the corresponding potential energy as given in **Eq. (2)**.The constants C_3 and C_4 ensure continuity between the linear and exponential regimes, where $C_3 = \frac{1}{2}\frac{E_1}{r_0}(r_y - r_0)^2 - \frac{r_0}{\alpha}$, and $C_4 = \frac{r_0}{\alpha}\exp\left[\frac{\alpha(r_s - r_y)}{r_0}\right] + \frac{1}{2}\frac{\beta}{r_0}(r_s - r_y)^2 + C_1(r_s - r_y) + C_3$. This formulation is inspired by the combination of β-sheet nanocrystals and amorphous protein domains as reported earlier[31].

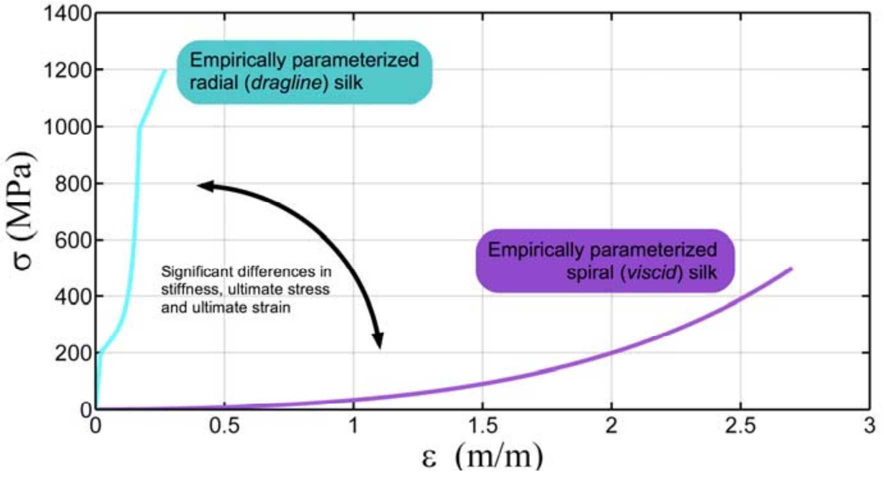

Figure S4 | Empirically parameterized stress-strain behaviours (implemented in Models B and C). Formulation for dragline and viscid silk behaviours derived from empirical parameters[1], providing accurate representation of experimental data of *Araneus diadematus.*

S3.2 Empirically parameterized dragline and viscid silk

To implement a more realistic web model in Models B and C we incorporate an empirical description of silk material behaviors. We use material behaviours from previously published experimental tensile tests on the silk of *Araneus diadematus*[1].

The functional form of the empirically parameterized dragline silk is identical to that of the atomistically derived dragline silk (described by **Eqs. (2), (S4)-(S5)**). The fitted empirical parameters are given in **Table S2.** To represent the J-shaped silk response seen in experimental studies and to maintain similarity with the previous derived dragline silk behaviour, a combination linear and exponential function is implemented:

$$\sigma(\varepsilon) = a \cdot \exp[\varepsilon] + b \cdot \varepsilon + c. \quad \text{(S6)}$$

The viscid silk behaviour is described by three parameters (*a, b,* and *c*) derived from three empirical properties (σ_b, ε_b, and E_init). Values of all parameters are given in **Table S2**.

For the implementation in our particle-spring model the stress-strain behaviour of viscid silk is converted to a force-displacement spring function given by:

$$F(r) = A_0 \cdot \sigma\big(\varepsilon(r)\big) \text{ and } \varepsilon(r) = \frac{r - r_0}{r_0}. \quad \text{(S7)}$$

Subsequently, the spring relation is used to determine the energy between all bonded pairs of particles, with the corresponding potential energy given in **Eq. (3)**.

Parameter	Value
Empirically parameterized dragline (radial) silk (Model C)	
Initial stiffness, E_1(empirical, ref.[1])	10,000 MPa
Exponential parameter, α	43.1
Tangent stiffness parameter, β	1,000 MPa
Final stiffness, E_2	2,087.4 MPa
Yield strain, ε_y (empirical, ref.[1])	0.02
Softening strain, ε_s	0.17
Ultimate (breaking) strain, ε_b (empirical, ref.[1])	0.27
Radial thread diameter	3.93 μm
Empirically parameterized viscid (spiral) silk (Models B and C)	
Ultimate stress, σ_b (empirical, ref.[1])	500 MPa
Ultimate strain, ε_b (empirical, ref.[1])	2.7
Initial Stiffness, E_init (empirical, ref.[1])	3 MPa
Exponential parameter, *a*	44.00 MPa
Tangent stiffness parameter, *b*	-41.00 MPa
Continuity constant, *c*	-44.00 MPa
Spiral thread diameter	2.40 μm

Table S2 | Empirically parameterized silk stress-strain behaviour parameters (used in Models B and C).

S3.3 Linear elastic model

A linear elastic material behaviour (displayed in materials such as carbon fibres[46], for example) to the silk behaviour is constructed simply by fitting a linear relation to the ultimate stress (σ_break) and ultimate strain (ε_b), where

$$\sigma(\varepsilon) = E_\mathrm{linear}\varepsilon \quad , \quad 0 \leq \varepsilon \leq \varepsilon_\mathrm{b}, \quad \text{(S8)}$$

and $E_{\mathrm{linear}} = \sigma_{\mathrm{break}}/\varepsilon_{\mathrm{b}}$ (**Fig. S5**).

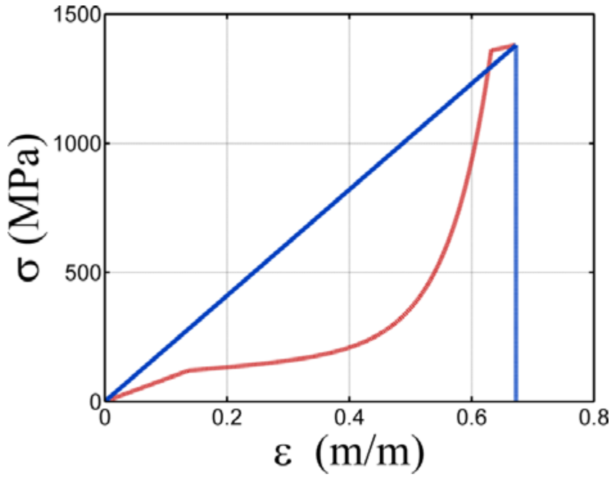

Figure S5 | Linear elastic constitutive behaviour atop the derived nonlinear silk behaviour (used in Models A' and C').

The stress-strain behaviour is converted to a force-displacement spring function by:

$$F(r) = A_0 \cdot \sigma\big(\varepsilon(r)\big) = \frac{E_{\mathrm{linear}} A_0}{r_0}(r - r_0), \tag{S9}$$

from which corresponding potential energy is determined as given in **Eq. (4)**.

Parameter	Value
Fitted to atomistically derived dragline silk (Model A')	
Stiffness, E_{linear}	2,050.6 MPa
Ultimate stress, σ_{break}	1,379 MPa
Ultimate strain, ε_{b}	0.6725
Fitted to empirically parameterized dragline silk (Model C')	
Stiffness, E_{linear}	4444.4 MPa
Ultimate stress, σ_{break}	1200 MPa
Ultimate strain, ε_{b}	0.27

Table S3 | Linear elastic stress-strain behaviour parameters (used in Models A' and C')..

S3.4 Elastic-perfectly-plastic model

An ideal elastic-perfectly-plastic material behaviour (a common simplifying assumption in ductile metal wires, for example) to the silk behaviour is constructed simply by fitting a linear relation to the ultimate stress (σ_{break}) and yield strain (ε_{y}), where $\varepsilon_{\mathrm{y}} = 0.5\varepsilon_{\mathrm{b}}$, where

$$\sigma(\varepsilon) = \begin{cases} E_{\mathrm{plastic}}\varepsilon \;, 0 \le \varepsilon < \varepsilon_y \\ E_{\mathrm{plastic}}\varepsilon_y \;, \varepsilon_y \le \varepsilon < \varepsilon_b \end{cases}, \tag{S10}$$

and $E_{\mathrm{plastic}} = \sigma_{\mathrm{break}}/\varepsilon_y = 2\sigma_{\mathrm{break}}/\varepsilon_b = 2E_{\mathrm{linear}}$ (**Fig. S6**). This behaviour reflects the simplest possible elastic-perfectly-plastic fit given an ultimate stress and strain.

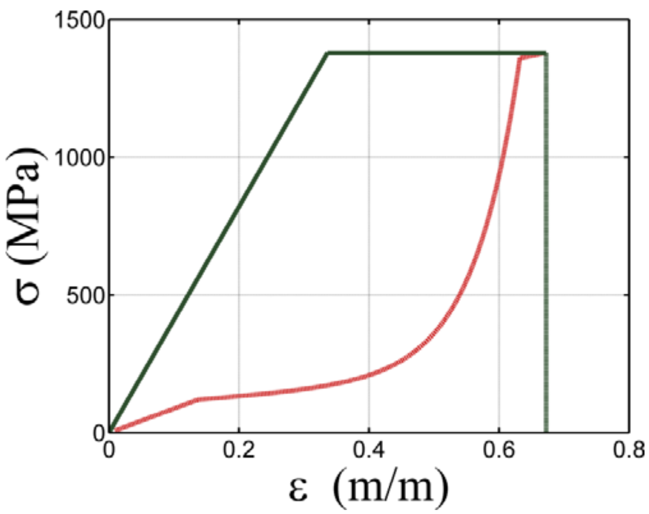

Figure S6 | Elastic-perfectly-plastic constitutive behaviour atop the derived nonlinear silk behaviour (used in Models A" and C").

The stress-strain behaviour is converted to a force-displacement spring function given by:

$$F(r) = A_0 \cdot \sigma\big(\varepsilon(r)\big) = \begin{cases} \frac{E_{\text{plastic}} A_0}{r_0}(r - r_0) & , \quad r_0 \le r < r_y \\ \frac{E_{\text{plastic}} A_0}{r_0}\left(r_y - r_0\right) & , \quad r_y \le r < r_b \end{cases}, \tag{S11}$$

from which corresponding potential energy is determined as defined in **Eq. (5)**.

Parameter	Value
Fitted to atomistically derived dragline silk (Model A")	
Stiffness, E_{plastic}	4,101.1 MPa
Yield stress, σ_{break}	1,379 MPa
Yield strain, ε_{y}	0.33625
Ultimate strain, ε_{b}	0.67250
Fitted to empirically parameterized dragline silk (Model C")	
Stiffness, E_{plastic}	8888.8 MPa
Yield stress, σ_{break}	1200 MPa
Yield strain, ε_{y}	0.135
Ultimate strain, ε_{b}	0.27

Table S4 | Elastic-perfectly-plastic stress-strain behaviour parameters (used in models A'' and C'').

S4. Application of local loading

We use a method inspired by Steered Molecular Dynamics[47] with a constant pulling velocity as the protocol for simulating local deformation of web. A harmonic spring driving force is applied to a selected particle group of magnitude:

$$F_{\text{SMD}} = K_{\text{spring}}(R - R_0), \tag{S12}$$

where $K_{\text{spring}} = 0.007$ N/m is the spring constant and R_0 is the current distance from the end of spring from a designated tether point. A constant velocity ($v = 0.02$ m/s) is prescribed which monotonously decrements the distance R towards the tether point (target coordinate). We select a target coordinate 10.0 m below the plane of the web to allow adequate deformation. The result is an applied load rate of 0.00014 N/s out-of-plane. The targeted load is applied to single spiral or radial thread, distributed over three particles (20 mm), representing, for example, a small piece of debris falling on the web. Applied force is compared with the maximum out-of-plane deformation of the web.

S5. Summary and comparison of results with completely empirically parameterized web models (Models C, C' and C")

The motivation for using the atomistically derived silk properties in Model A is the linking previously discovered molecular characteristics of silk with the web-scale functionality and performance. To provide a more realistic web model tied to a specific spider species, we implement the empirically parameterized silk behaviors (Model C, as described in **Section S3**). Linear elastic (Model C') and elastic-perfectly-plastic (Model C") behaviors are fitted based on the ultimate stress and strain of the empirically parameterized dragline silk. We then subject Models C' and C'' to the same loading conditions (pulling a single radial thread, pulling a single spiral thread) for comparison with the results obtained with Models A, A' and A''.

The results are similar to those attained with the atomistically derived models (Models A, A', and A") as depicted in **Figure S7**, albeit with reduced maximal forces and displacement. In both Models A and C (and their derivatives), the natural silk behavior with its softening-stiffening stress-strain behavior results in the lowest load to failure, followed by the linear elastic and elastic-perfectly-plastic responses. The empirical material models consistently fail at both lower loads and lower displacement. The decrease in load is due to the natural geometry of the web, where the applied load is normal to the web plane. Thus, the component of the force transferred along the loaded thread is proportional to $1/\sin(\theta)$. As the extensibility of the silk material behavior implemented in Model C is lower than on Model A (less deformation and θ for a given load), a lower force at failure is anticipated.

The empirically parameterized material behaviors in Models C, C' and C'' result in the poorest performance in terms of achieved maximum force and displacement. Very little force is transferred to the spiral threads due to the substantial difference in stiffness. This differs from the results from model A, as the spiral threads are dramatically more compliant (Model C) than the linear elastic (Model C') or elastic-perfectly-plastic (Model C") spiral threads implemented. Thus, the web system is intrinsically weaker, resulting in a decrease in ultimate force and displacement upon failure. This supports the notion that the spiral threads function in non-structural roles and the applied load is carried almost entirely by the loaded radial. Indeed, it has been shown that for webs and similar compliant structures the path with the greatest stiffness carries the greatest load[18]. We find that increasing the difference in relative stiffness between radial and spiral threads results in less force transfer to the adjacent spirals when a radial thread is subject to loading. This disparity in stiffness is not as great in the corresponding linear elastic and elastic-perfectly-plastic models.

Most importantly, we also compare the damage between material behaviors, to test if the results follow the same trend as seen in Model A and its derivatives. Again, we see that the natural nonlinear softening-stiffening silk (Model C) results in the least amount of damage, and highly localized about the area of the loaded radial thread. The key result and in agreement with the results obtained with Model A is that the damage increases for the linear elastic (Model C') and even more for the elastic-perfectly-plastic (Model C") behaviors. This follows the same trend as the previous models (damage in Model A < Model A' < Model A"). In Model C, C' and C'' we see that more damage is inflicted than in Model A and its derivatives, potentially attributed to the more brittle behavior of the web due to lower extensibility.

The introduction of the above empirically derived silk is only reflective of a single species. Yet, the web performance (in comparison to linear elastic and elastic-perfectly-plastic cases) is remarkably similar between the atomistically derived and empirically parameterized cases. This confirms that while the atomistically derived constitutive behavior may not be an exact representation of silk of a particular species, the performance of the web relies on the differences in the shape of the stress strain curves, and not the absolute extensibility or strength of the silk threads. It is apparent that the nonlinear stiffening begets web robustness, where local failure and repair is preferential to system-level behaviour.

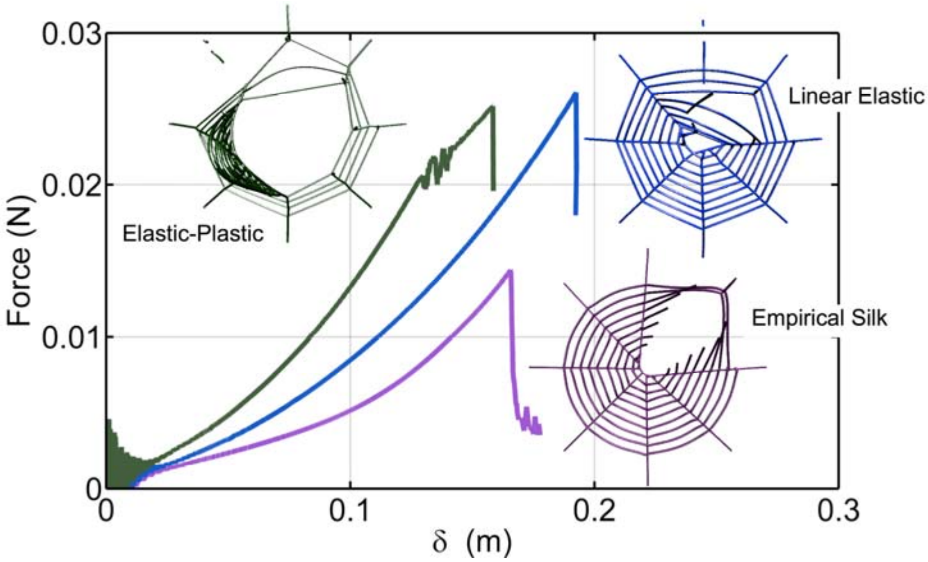

Figure S7 | Force-displacement plots of web models with empirical silk (Model C), linear elastic silk (Model C') and elastic-perfectly-plastic silk (Model C''), pulling a radial thread, for empirically parameterized material behaviors with snapshots post-failure. Failure/damage is highly localized for empirical (nonlinear stiffening) silk and increases from linear elastic to elastic-perfectly-plastic material behaviours. The introduction of relatively stiffer elements (empirically parameterized dragline threads) results in less force transfer to the extensible viscid silk. As a result, less silk threads are engaged upon radial thread loading and the combination of stiff dragline plus extensible viscid results in poorer performance (in terms of max load and displacement) when compared to purely linear elastic or elastic-perfectly-plastic constitutive laws (with the same stress and strain as the empirical dragline silk). Note that both these materials would have greater toughness than natural silk. The results agree with the findings shown in Fig. 2 and the relations depicted in Fig. 3 and provide evidence for the generality of the findings.

Comparing the pulling of spiral threads with the pulling of radial threads to corroborate with our *in situ* tests and photographs, we find that the deformation mechanisms concur with experimental images. As seen in models A and B, pulling a radial thread results in extensive deformation of the web. The less extensible and inherently stiffer dragline silk results in a more rigid system dominated by the radial thread behavior. As before, in Model C there is extensive web deformation when a radial thread is pulled and little force is transferred to the spiral threads. Loading a spiral thread results in highly localized deformation with little response from the remainder of the web. This is due to (*i*) the relative size of the spiral threads (less force to transfer) and (*ii*) the relative stiffness of the radial thread (less displacement). Note that when force is sufficient to break the spiral (calculated knowing the thread area and ultimate stress), the resulting force and maximum stress in radial threads is not sufficient to cause yielding. With the empirically parameterized Model C (with relatively stiffer radial dragline silk and extensible spiral viscid silk) pulling a spiral thread limits the deformation to the thread being loaded, effectively pinned in place by the stiffer, anchoring radial threads. This closely resembles the mode of deformation reflected in our photographs of physical webs (**Fig. 1e-f**), whereas the initial atomistically derived spiral silk induced more (albeit still local) deformation.

S6. Work to break threads

Here we compare the response of both radial and spiral thread pulling in terms of ultimate load and work applied (using Models A and B). For the derived dragline model (Model A, where the spiral threads behave similarly to the radials), we find ultimate loads of 29.1 mN and 11.9 mN for the radial and spiral pulling respectively. Note the ultimate stress both threads is equivalent, and ultimate force is thus determined by the cross-sectional area. The ratio of ultimate loads ($29.1/11.9 \approx 2.45$) is equal in magnitude to the ratio of areas ($(3.93/2.40)^2 \approx 2.68$) as expected. For radial threads (dragline silk), the work required to induce failure via out-of-plane spring controlled loading is calculated to be approximately 3.15 mJ, whereas the work required for dragline silk spiral threads is 1.09 mJ.

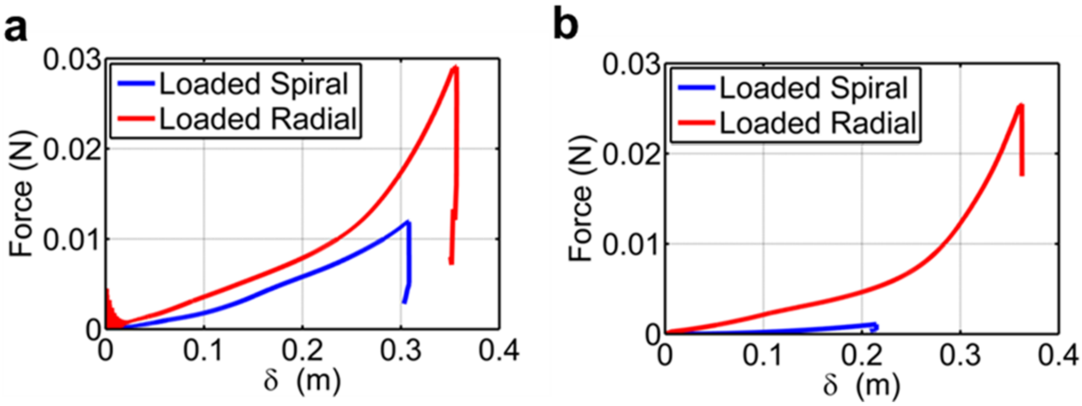

Figure S8 | Applied force versus displacements for different models. a, Plot of applied force versus thread displacement for both spiral thread loading and radial thread loading (Model A). b, Plot of applied force versus thread displacement for compliant spiral thread loading compared to radial thread loading (Model B).

The two force deflection curves for radial pulling and spiral pulling clearly indicate that while they may be equivalent in terms of toughness *per mass*, viscid threads require much less energy to break. For Model B, we find ultimate loads of 25.5 mN and 1.1 mN for the radial and spiral pulling respectively. For radial threads, the work required to induce failure is calculated to be approximately 2.33 mJ, whereas the work required for viscid silk spiral threads is only 0.110 mJ. Here, there is less force and energy required to break a radial thread compared to the all previous case as there is less resistance contributed by the weaker spiral threads. It is noted that, as the spiral threads are much weaker, there is little force transfer to the web structure when a spiral thread is loaded, thereby limiting deformation to a single thread. In the cases considered here (Models A and B), the overall web performance is dominated by the strength of the radial dragline silk threads. Although more extensible, viscid silk threads are weaker than their dragline counterparts, and thus transfer less force and dissipate less mechanical energy under load. The spiral viscid threads are relegated to non-structural roles (functioning as capturing prey) and are expendable in terms of structural performance and robustness. From these results, it is anticipated that removal of multiple spiral elements would have little effect on the overall web performance.

S7. Web performance under addition of random defects

We find that the removal even of a large segment of spiral threads has very little effect on the failure mechanism of the web as a whole and that the overall force-displacement behaviour remains marginally affected. As the defect density increases to 5%, the maximum force before failure changes by no more than 3% and the maximum displacement decreases by no more than 4%. Clearly, spiral threads play a minimal role in the failure mechanism of the full web structure, supporting the approximation of radial-type behaviour for spiral threads. Shifting the defect location closer to the site of load application has a similarly minimal effect for spiral thread defects. On the other hand, radial defects have a much more pronounced effect as the location of the removed radial approaches the loading site: maximum force and displacement decrease by approximately 15% and 50%, respectively, with increasing proximity to site of load. These observations suggest that the load is locally concentrated in the radial thread where it is applied and in the adjacent radial threads. The existence of a web-like mesh structure is critical as the failure of few elements does not lead to the catastrophic breakdown of the material as shown in **Fig. 1c**.

S8. Global loading (wind load)

To model the effect of wind, we utilize the effect of drag on the silk threads, similar to the wind drag on cable bridges, for example Ref. [48]. The static drag wind load on a stay cable is written as:

$$F_{\mathrm{d}} = \frac{1}{2}\rho_{\mathrm{air}} U^2 C_D A, \tag{S13}$$

where ρ_{air} is the air density, U the mean wind speed, A the reference area of the silk thread ($A = r_0 \times$ diameter) and C_{D} the drag coefficient in the along-wind direction (conservatively taken as 1.2, typical value for structural wires and cables[48]). Within the simulation, this drag force is converted to a constant acceleration driving field:

$$a_i = \frac{F_{\mathrm{wind}}}{m_i} = \frac{1}{2}\frac{\rho U^2 C_D A}{m_i} \quad , \tag{S14}$$

where different accelerations are applied to either radial or spiral segments to account for different in mass (proportional to cross sectional area, where $m_i = \rho_{\mathrm{silk}}\frac{1}{4}\pi {d_i}^2 r_0$). We thus define the normalized drag force (applied to all silk threads) as:

$${F_{\mathrm{d}}}^n = \frac{1}{2}\rho_{\mathrm{air}} U^2 C_D. \tag{S15}$$

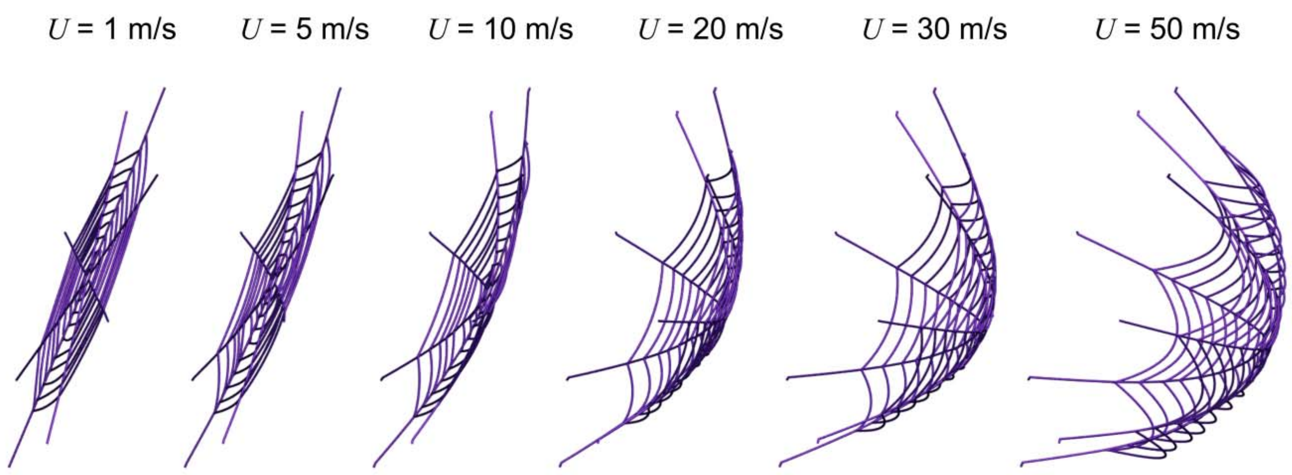

Figure S9 | Web response under increasing wind speeds (results of Model B shown).

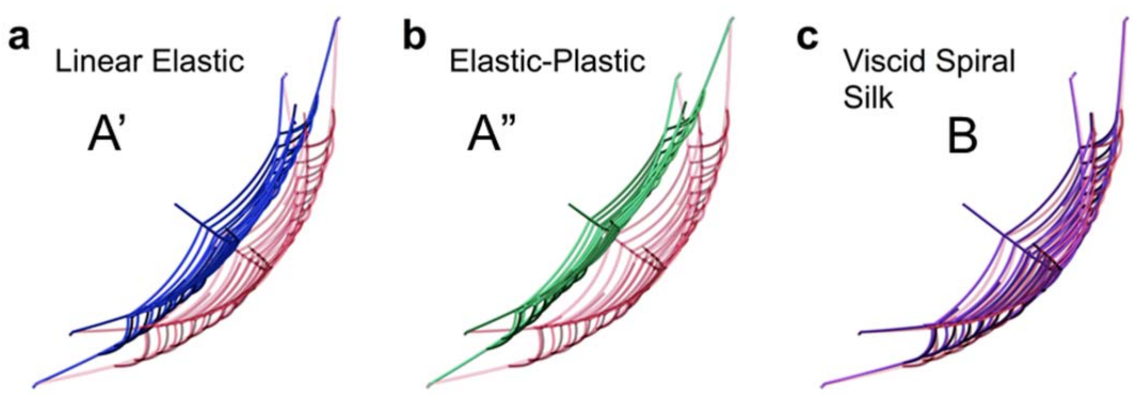

Figure S10 | Visualizations of web deflection for all material models under a constant wind speed of 20 m/s. a, linear elastic (Model A'), b, elastic-perfectly-plastic (Model A"), and c, results of the viscid spiral thread model (Model B). In all cases the atomistically derived model (Model A; shown in red) is used as basis of comparison.

The web is subject to constant loading with equivalent wind speeds ranging from 0.5 to 70 m/s (reaching up to strong hurricane level winds), which the maximum deflection was measured (relative to the anchoring points). The load is applied for 100 seconds (**Fig. S9** and **S10**). The load cases are repeated for all four material models (Models A, A', A'', and B). The results are summarized in **Fig. S11**. Regardless of material behaviour, the web structure can withstand hurricane level wind speeds (speeds of approximately 40 m/s are defined as Category 1 hurricanes[49]). Similarly, all webs fail at wind speeds exceeding approximately 60 m/s (Category 4 hurricane level). It is noted that while the wind loading applied here is ideal (symmetric, homogenous, and constant), the results indicate a large resistance to wind-type loading due to the combined small mass and cross-section of the web silk elements. The system-level deflection curves are indicative of the implemented constitutive silk behaviour. Here, the elastic-perfectly-plastic model (A") depicts the least deflection, as it has the highest stiffness, followed by the linear elastic response (A'), and finally the silk models (both Model A and B reflect nominal differences). The behaviour of the radial threads (which ultimately transfer the wind load to the anchoring points) dominates the behaviour of the web itself.

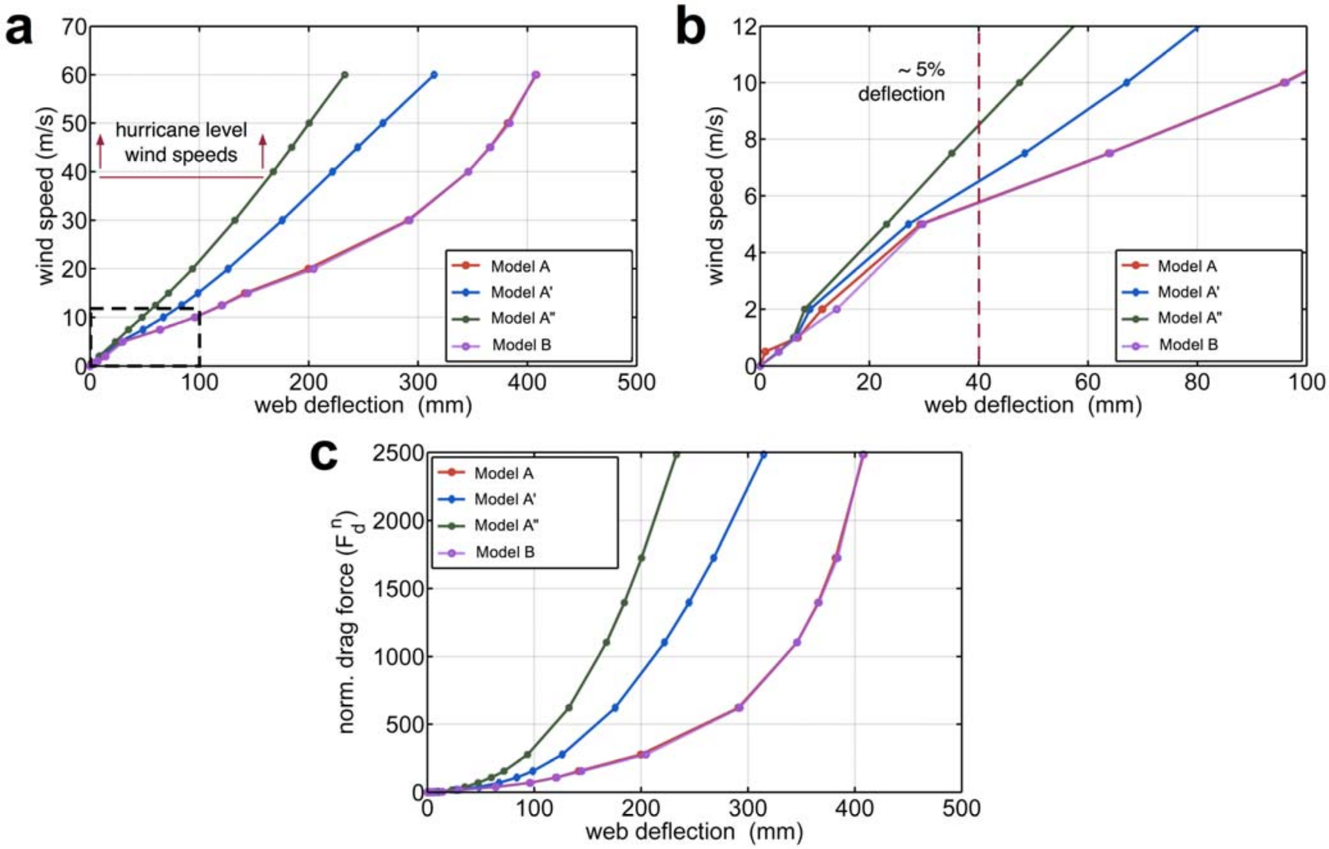

Figure S11 | Summary of results for the global (wind) loading cases. a, Wind speed verses web deflection for all wind speeds applied. Failure of all webs occurs at web speeds exceeding 60 m/s (classified as Category 4 hurricane wind speeds). Web response is dominated by the constitutive law of the radial threads, with nominal differences when the more extensible, empirically derived viscid silk is implemented as spiral threads. b, Expanded view of low wind speeds (indicated in panel a, indicating radial yielding at wind speeds exceeding approximately 5 m/s. All models maintain structural integrity below this nominal speed. c, Web deflection plotted against normalized drag force.

This wind load investigation leads to three main findings:

(1) The nonlinear stiffening behaviour is disadvantageous to web performance subject to large distributed forces. Yielding occurs in multiple threads simultaneously, leading to large web deflections under "extreme" wind loading.

(2) The initial stiffness of dragline silk provides structural integrity under functional, or operational, conditions (expected typical wind speeds). Web rigidity is maintained and deflection is comparable to the traditional engineered material behaviours (linear elastic and elastic-perfectly-plastic).

(3) The greater extensibility of viscid silk (versus dragline silk) only nominally affects the system-level response, as the load is transferred to the anchoring points via the radial threads, which are much stiffer.

These findings suggest that whereas the nonlinear stiffening response of dragline silk is crucial to reduce damage of localized loading, it is disadvantageous to global (distributed) loading scenarios. Yielding caused by the high wind loading results in web displacements that could cause large areas of the sticky catching-spiral to impact surrounding environment (such as vegetation), which would result in the large-scale destruction of a web. However, under moderate wind loading, the linear regime of the dragline silk dominates behaviour, and silk performs as well as the other material behaviours. The wind load cases illustrate that the initial stiffness of the dragline provide structural integrity under such "global" loading conditions. If this loading becomes "extreme" there is no benefit, and the silk yields. Presumably, what is considered "extreme" or "normal" environmental is dependent on the locale of the spider, and our approach can systematically link variation in the mechanical properties between silks of different species to such environmental loading conditions. For the current silk model, the yield occurs at wind speeds exceeding 5 m/s, defining a reasonable regime of operational wind speeds.

S9. Distribution of deformation states in the web

Figure S12 depicts the potential energy (PE) distribution for atomistically derived silk behaviour (Model A). Stress distributions depicted in **Figure 2a** are calculated by definitions of PE giving by Equations (2) to (5). We find that stress is localized on the radial thread where load is applied directly. In such compliant structures, it is anticipated that the stiffest elements resist the greatest load. The cooperative action of a stiffening structural member (the radial silk thread under load) with yielding (or softening) of ancillary members results in a localization of elastic resistance. Concurrently, adjacent radials reveal a partially stiffened state – immediately after failure, load is redistributed between these two adjacent threads, keeping the rest of the web intact and functional. The radial thread where load is applied incurs severe stiffening. Sections of the web removed from loading undergo limited deformation and strain.

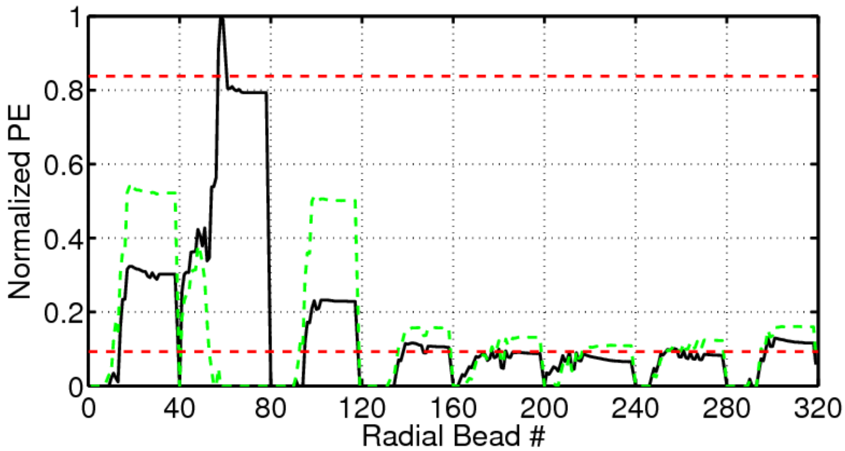

Figure S12 | Normalized potential energy (PE) distribution considered for radial threads (radial threads consist of 40 particle (bead) intervals; loaded radial beads from 41-80), for natural silk behaviour (Model A). The plot depicts energy distribution just prior and immediately after web fracture (solid black and dashed green lines, respectively). Energy is normalized with respect to maximum potential energy at failure. Dashed red lines indicate potential energy at which yielding occurs. Prior to failure, the majority of potential energy is associated with the radial thread under load. Most threads have been strained just up to the point of yield, facilitating load concentration at the stiffening, loaded thread. Following failure, load is transferred to the adjacent threads (until loaded thread is completely detached from the web structure) but threads far from the load still experience little increase in strain

S10. Quantized Fracture Mechanics (QFM) analysis

To investigate the failure of the webs, we implement a modified formulation of fracture mechanics, accounting for the discrete nature of webs, called Quantized Fracture Mechanics (QFM)[51,52,53]. QFM is relevant to the fracture of small structures such as nanotubes, nanowires, and nanoplates and was developed to handle the discreteness of matter at the atomistic scale. Here we apply QFM to model the results of the simulations and experimental studies that show that nonlinear material behaviour of natural silk begets large web robustness against localized attacks and generalize the observations for different materials and structures. Classical Linear Elastic Fracture Mechanics (LEFM) cannot reach this goal since it is based on linear elasticity and on the assumption of a continuum, which is not valid in a discrete mesh-like structure such as a spider web. We consider the simplest structure that will give us general insights, an elastic plate with a crack of length $2a$ subjected at its centre to a pair of applied forces per unit width, F. The stress-intensity factor at the crack tips is:

$$K_I = \frac{F}{\sqrt{\pi a}} \tag{S16}$$

According to LEFM the crack will start to propagate when the stress-intensity factor equals the material fracture toughness, K_{IC}, thus for an initial crack length shorter than:

$$a_C = \frac{1}{\pi}\left(\frac{F}{K_{IC}}\right)^2 \tag{S17}$$

(here quasi-static crack propagation is stable, different from the Griffith case). According to QFM and in contrast to classical theory the crack will propagate not when $K_I = K_{IC}$, but when

$$K_I^* = \sqrt{\frac{1}{q}\int_a^{a+q} K_I^2(a)\mathrm{d}a} = K_{IC},$$

and thus when the applied force per unit width is:

$$F = \frac{K_{IC}\sqrt{\pi q}}{\sqrt{\ln\left(1+\frac{q}{a_C}\right)}} \quad . \tag{S18}$$

In Eqs. (S17) and (S18) q is the fracture quantum, representing the characteristic size of the structure; and here q is the size of the web's mesh spacing and a measure of the discreteness of the system. Comparing Eqs. (S17) and (S18) we note that the prediction of QFM is equivalent to that of LEFM if an equivalent toughness $K_{IC}^{(q)}$ is assumed in the classical LEFM approach:

$$K_{IC}^{(q)} = \frac{K_{IC}}{\sqrt{\frac{a_C}{q}\ln\left(1+\frac{q}{a_C}\right)}} \cong K_{IC}\left(1+\frac{q}{4a_C}\right). \tag{S19}$$

Eq. (S19) shows that in the case of a localized targeted load (in contrast to the less critical case of distributed loading) the discrete nature of the structure helps in increasing its robustness since $K_{IC}^{(q)} \propto q$. This implies that the critical crack length a_C is reduced due to the discrete nature of the structure, as suggested by the asymptotic limit given by Eq. (S18):

$$a_C \cong \frac{1}{\pi}\left(\frac{F}{K_{IC}}\right)^2 - \frac{q}{2}. \tag{S20}$$

In order to generalize the concept to different constitutive laws that define the unique relationship of how stress σ versus strain ε behaves, we consider a general nonlinear stress-strain law in the form of a power law $\sigma \sim \varepsilon^{\kappa}$.

Here $\kappa < 1$ denotes elastic-plastic behaviour (nonlinear softening), $\kappa = 1$ linear elasticity, and $\kappa > 1$ represents a nonlinear stiffening material. The limiting cases are $\kappa = 0$ (perfectly plastic material) and $\kappa = \infty$ (perfectly nonlinear stiffening material). The power of the stress-singularity at the crack tip will be modified from the classical value of 1/2 to[50]:

$$\alpha = \frac{\kappa}{\kappa+1}, \tag{S21}$$

and we define α as the nonlinearity parameter (linear elastic case when $\alpha = 1/2$, stiffening when $\alpha \rightarrow 1$ and softening when $\alpha \rightarrow 0$). Thus, the singularity changes similarly to what occurs at the tip of a re-entrant corner (edge cut)[51]. Based on QFM theory[52] we predict the critical force per unit width $F^{(\alpha)}$ for a nonlinear material described by the exponent α, as a function of the critical force per unit length for linear elasticity ($F^{(1/2)}$) and perfect plasticity ($F^{(1)}$):

$$\frac{F^{(\alpha)}}{F^{(1)}} = \left(\frac{F^{(1/2)}}{F^{(1)}}\right)^{2\alpha}. \tag{S22}$$

Defining $F^{(1)} =: f$ as the breaking force per unit width of a single structural element (a spider silk thread), Eq. (S18) becomes:

$$F = f\left(\frac{K_{IC}}{f}\right)^{2\alpha}\left(\frac{\pi q}{\ln\left(1+\frac{q}{a_C}\right)}\right)^{\alpha}. \tag{S23}$$

In the limit of $q \rightarrow 0$, Eq. (S23) defines the equivalent fracture toughness due to the nonlinearity of the stress-strain law:

$$K_{IC}^{(\alpha)} = K_{IC}^{2\alpha}\left(\frac{f}{\sqrt{\pi a}}\right)^{1-2\alpha}. \tag{S24}$$

Since by definition $F > f$ during dynamic failure, Eq. (S24) suggests that $K_{IC}^{(\alpha)}$ increases with α, and accordingly the emergence of nonlinear stiffening as $\alpha \rightarrow 1$ presents a toughening mechanism. Moreover, Eq. (S20) becomes:

$$a_C = \frac{1}{\pi}\left(\frac{F}{f}\right)^{\frac{1}{\alpha}}\left(\frac{f}{K_{IC}}\right)^2. \tag{S25}$$

More generally, mixing discreteness and nonlinearity gives an equivalent structural[54] fracture toughness of:

$$K_{IC}^{(\alpha,q)} = \frac{f}{\sqrt{\pi a_C}}\left(\frac{K_{IC}}{f}\right)^{2\alpha}\left(\frac{\pi q}{\ln\left(1+\frac{q}{a_C}\right)}\right)^{\alpha} \tag{S26}$$

from where an interaction between discreteness and the nonlinearity of the stress-strain law can be deduced. Asymptotically, the critical crack length becomes:

$$a_C = \frac{1}{\pi}\left(\frac{F}{f}\right)^{\frac{1}{\alpha}}\left(\frac{f}{K_{IC}}\right)^2 - \frac{q}{2}. \tag{S27}$$

Behaviour	Corresponding Model	Total Broken Elements	Spiral Broken Elements	Radial Broken Elements
Linear Elastic $\alpha_l = 0.50$	A'	7 (simulation) 7 (QFM)	3 (simulation) 3 (QFM)	4 (simulation) 4 (QFM)
Elastic-Perfectly-Plastic $\alpha_p \approx 0.30$	A"	24 (simulation) 24 (QFM)	12 (simulation) 11 (QFM)	12 (simulation) 13 (QFM)
Stiffening $\alpha_h \approx 0.90$	A	4 (simulation) 4 (QFM)	0 (simulation) 0 (QFM)	4 (simulation) 4 (QFM)
Natural spider web (composed of dragline and viscid silk) $\alpha_d \approx 0.90$ $\alpha_v \approx 0.75$	B	4 (simulation) 5 (QFM)	0 (simulation) 1 (QFM)	4 (simulation) 4 (QFM)

Table S5 | Comparison between our web simulations and predictions from Quantized Fracture Mechanics (QFM) theory for the failure of webs composed of materials with different stress-strain laws. The results clearly show the significant increase of the extension of damage for elastic-perfectly-plastic softening material behaviour, and minimal damage for the natural stiffening behaviour.

The QFM predictions of Eqs. (S26) and (S27) suggest strategies in the impact mitigating design of spider web inspired structures. Most importantly, both the discreteness (measured by q) and nonlinear stiffening (measure by α) represent toughening mechanisms against failure under localized loading. Eq. (S27) shows that the damaged zone after failure has a characteristic size that diverges as the exponent α is decreased (*i.e.*, $\alpha \rightarrow 0$ so that the material approaches a softening stress-strain behaviour). In order to take the discreteness of the structure into account we introduce Eq. (S17) into Eq. (S22) and find for the ratio of damaged material:

$$\varphi(\alpha) = \left(\frac{a_C^{(\alpha)}}{a_C^{(1)}}\right)^2 \tag{S28}$$

Since by definition $a_C^{(1)}$ represents the overall size of the entire structure, $\varphi(\alpha)$ represents the damaged area fraction of the structure after failure. Further, by expanding Eq. (S28) we arrive at

$$\left(\frac{a_C^{(\alpha)}}{a_C^{(1)}}\right)^2 = \left(\frac{a_C^{(1/2)}}{a_C^{(1)}}\right)^{4\alpha} = \left(\varphi^{(1/2)}\right)^{2\alpha} = S^{2\alpha} = \varphi(\alpha). \tag{S29}$$

Herein $S = \varphi^{(1/2)}$ is a system-dependent constant that represents the ratio of damaged material associated with the linear elastic behaviour. The parameter S reflects material properties such as fracture toughness, system geometry (*i.e.* crack width), and applied loading conditions. Considering a heterogeneous structure composed by n different materials (such as dragline and viscid silks as found in natural orb webs), with volumetric ratios v_i ($\sum_{i=1}^{n} v_i = 1$) and described by n different constitutive law exponents α_i, we expect ratios of damaged materials in the phases i equal to:

$$\varphi^{(i,\alpha_i)} = \left(\varphi^{(i,1/2)}\right)^{2\alpha_i} = \left(S^{(i)}\right)^{2\alpha_i}, \tag{S30}$$

and in the entire structure of:

$$\varphi = \sum_{i=1}^{n} \varphi^{(i,\alpha_i)} v_i. \tag{S31}$$

The "structural robustness" Ω is defined as the fraction of surviving material in the structure after failure has occurred:

$$\Omega = 1 - \varphi = 1 - S^{2\alpha}. \quad \text{(S32)}$$

The result of Eq. (S32) is depicted in **Fig. 3** for a single material structure. We recognize that fixing all other variables, the larger the material nonlinearity parameter α the larger the structural robustness. Therefore, generally and independent from the specific material behaviour of silk, a more pronounced the material stiffening with strain, the larger the structural robustness as failure is increasingly localized, thus resulting in failure of a minimal number of elements in a discrete mesh-like structure[52].

We apply the theory to three different hypothetical homogenous structures (Models A, A', and A") as well as to the heterogeneous web (Model B), all composed of 8×10=80 radials and 8×10=80 spirals. The considered materials for the homogeneous structures are linear elastic ($\alpha_l = 0.50$), elastic-perfectly-plastic (best fit $\alpha_p \approx 0.30$) and nonlinear stiffening (*i.e.* atomistically derived dragline silk, best fit $\alpha_h \approx 0.90$), whereas for Model B we consider the radials as composed by dragline silk ($\alpha_d \equiv \alpha_h \approx 0.90$) and the spirals as composed by viscid (capture) silk (best fit $\alpha_v \approx 0.75$). The comparison between the simulations and QFM predictions is reported in **Table S5** and shows good agreement. Note that in the simulations we always observed that at least 4 radial elements are broken (considering the radial as independent units, *i.e.* in number 8, Eq. (S30) would roughly result in 2), as a consequence of the application of the load directly on a radial element; thus, to take this cooperative mechanism into account, of the radial elements that belong to the same radial, our final prediction is the maximum between this number and the one that resulted from application of Eq. (S30). As demonstrated in the theoretical analysis**,** our findings generally hold for other materials (including nanostructures) in which the material's stress-strain behaviour dictates functionality beyond limit parameters, such as the ultimate strength.

S11. Simulation software and computational equipment

The simulations are performed using the modelling code LAMMPS[53] (http://lammps.sandia.gov/) modified to allow the constitutive behaviours described herein. Web models are simulated using molecular dynamics formulations, with an *NVE* ensemble at finite temperature (300 K) (where *N*=constant particle number, *V*=constant simulation volume, *E*=constant energy). A small damping force is introduced to dissipate kinetic energy (approximately 1 mN-s-m^{-1}) for all simulations. The web structure is minimized and equilibrated for 10 seconds (100,000 time steps) prior to the addition of any load. The calculations and the analysis were carried out using a parallelelized LINUX cluster at MIT's Laboratory for Atomistic and Molecular Mechanics (LAMM). Visualization has been carried out using the Visual Molecular Dynamics (VMD) package[54].

Supplementary references

34 Gosline, J. M., Demont, M. E. & Denny, M. W. The Structure and Properties of Spider Silk. *Endeavour* **10**, 37-43 (1986).

35 Vollrath, F. Strength and structure of spiders' silks. *Reviews in Molecular Biotechnology* **74**, 67-83 (2000).

36 Swanson, B. O., Blackledge, T. A., Beltran, J. & Hayashi, C. Y. Variation in the material properties of spider dragline silk across species. *Applied Physics a-Materials Science & Processing* **82**, 213-218 (2006).

37 Opell, B. D. & Bond, J. E. Changes in the mechanical properties of capture threads and the evolution of modern orb-weaving spiders. *Evolutionary Ecology Research* **3**, 567-581 (2001).

38 Elices, M. *et al.* Mechanical Behavior of Silk During the Evolution of Orb-Web Spinning Spiders. *Biomacromolecules* **10**, 1904-1910 (2009).

39 Kohler, T. & Vollrath, F. Thread Biomechanics in the 2 Orb-Weaving Spiders Araneus-Diadematus (Araneae, Araneidae) and Uloborus-Walckenaerius (Araneae, Uloboridae). *Journal of Experimental Zoology* **271**, 1-17 (1995).

40 Lin, L. H. & Sobek, W. Structural hierarchy in spider webs and spiderweb-type system. *The Structural Engineer* **76**, 59-64 (1998).

41 Denny, M. Physical-Properties of Spiders Silk and Their Role in Design of Orb-Webs. *Journal of Experimental Biology* **65**, 483-506 (1976).

42 Zschokke, S. & Vollrath, F. Web Construction Patterns in a Range of Orb-Weaving Spiders (Araneae). *European Journal of Entomology* **92**, 523-541 (1995).

43 Romer, L. & Scheibel, T. The elaborate structure of spider silk Structure and function of a natural high performance fiber. *Prion* **2**, 154-161 (2008).

44 Heim, M., Keerl, D. & Scheibel, T. Spider Silk: From Soluble Protein to Extraordinary Fiber. *Angewandte Chemie-International Edition* **48**, 3584-3596 (2009).

45 Heim, M., Romer, L. & Scheibel, T. Hierarchical structures made of proteins. The complex architecture of spider webs and their constituent silk proteins. *Chemical Society Reviews* **39**, 156-164 (2010).

46 Zhou, Y. X. & Xia, Y. M. Experimental study on the strength loss of carbon fiber in unidirectional carbon/aluminum composites. *Journal of Materials Science Letters* **21**, 743-746 (2002).

47 Sotomayor, M. & Schulten, K. Single-molecule experiments in vitro and in silico. *Science* **316**, 1144-1148 (2007).

48 Poulin, S. & Larsen, A. Drag loading of circular cylinders inclined in the along-wind direction. *Journal of Wind Engineering and Industrial Aerodynamics* **95**, 1350-1363 (2007).

49 The Saffir-Simpson Hurricane Wind Scale. *National Hurricane Center, National Weather Service*, (2011).

50 Rice, J. R. & Rosengren, G.F.. Plane Strain Deformation near a Crack Tip in a Power-Law Hardening Material. *Journal of the Mechanics and Physics of Solids* **16**, 1-12 (1968).

51 Carpinteri, A. & Pugno, N. Fracture instability and limit strength condition in structures with re-entrant corners. *Engineering Fracture Mechanics* **72**, 1254-1267 (2005).

52 Pugno, N., Carpinteri, A., Ippolito, M., Mattoni, A. & Colombo, L. Atomistic fracture: QFM vs. MD. *Engineering Fracture Mechanics* **75**, 1794-1803 (2008).

53 Plimpton, S. J. Fast parallel algorithms for short-range molecular dynamics. *Journal of Computational Physics* **117**, 1-19 (1995).

54 Humphrey, W., Dalke, A. & Schulten, K. VMD: Visual molecular dynamics. *Journal of Molecular Graphics* **14** (1996).

and offered naval protection for the reconstruction of the base. The incident was quickly brushed off as a misunderstanding, but relations had been strained. Less than a decade later, the international Antarctic Treaty set aside the territorial disputes that fuelled such skirmishes, and effectively handed the continent over to science.

Such lessons from history are a useful reminder that Antarctica has not always been the research utopia that it is now, and that it took the resolution of real tensions and difficulties to render the incident at Hope Bay a curious historical footnote rather than a sign of things to come. There are also lessons here for the Arctic; specifically, how to manage the region as tensions rise over its oil and gas reserves that are driving greater exploration as the sea ice dwindles.

As we report on page 13, the drive to locate and exploit fossil-fuel resources in the Arctic continues apace. At a meeting in the Norwegian city of Tromsø last week, executives from oil and gas firms queued up to boast of the riches the region could offer to their companies and shareholders.

Politicians can see the potential too. Ola Borten Moe, Norway's minister of petroleum and energy, last month awarded 26 new production licences for mature offshore oil areas in the Norwegian Sea and Barents Sea. New oil and gas development is under way off Norway, Greenland, Alaska and the northern coast of Russia. According to a much-quoted 2008 estimate from the US Geological Society, about 13% of the world's remaining technically recoverable oil, and up to 30% of its gas, is in the Arctic — most of it under the Arctic Ocean.

Yet, in the wake of the April 2010 Deepwater Horizon oil spill in the Gulf of Mexico, the environmental risks of such a dirty industry expanding into a pristine environment are obvious. Two environmentalists who envisaged the impact of a spill in the Arctic called it "A frozen hell" in a *Nature* article published on the first anniversary of the Deepwater Horizon disaster (J. Short and S. Murray *Nature* **472,** 162–163; 2011).

Such an accident would be a global catastrophe. What can be done, on a worldwide scale, to prevent an Arctic spill from happening, and to ensure a rapid and coordinated response to mitigate the impact if it did? How can scientists contribute?

Common wisdom at this point tends to highlight the difficulties of political collaboration and governance in the Arctic, given the overlapping territorial claims and the lack of an agreement similar to the Antarctic Treaty. It is true that the Arctic Council — which represents the nations and people of the Arctic Circle — has so far done little to answer critics who dismiss it as a toothless talking shop.

Formed in its present state only in 1996, the council did, however, produce its first legally binding agreement between nations last year, which sets out the responsibilities of its members to contribute to search-and-rescue activities. And it has now set up a task force to explore whether a similar agreement could be reached on how to prevent, prepare for and respond to Arctic oil pollution.

"The high north is no longer a place of interest to only a select few."

That process could yet be controversial — Greenland has suggested it should include a formal liability and compensation scheme — and it is in its early stages. The group held only its second meeting in St Petersburg, Russia, in December, but it is scheduled to report back on the various options next year.

If the council is serious about the exercise — which it should be, given that its members will be on the front line of any Arctic spill — then it could offer a timely and useful contribution. To achieve this potential, it should open up the process as widely as possible, and follow through on plans to involve in its discussions experts from scientific and environmental fields, as well as representatives from the offshore oil and gas industry. It should aim high, and look to create a binding agreement that is legally enforceable.

If that means the council going beyond its comfort zone, then it could seek wider international support for such a move. Several non-Arctic nations, including China and India, are already eyeing the region and its opportunities, and have asked for representation on the council.

Their requests have triggered debate and some resistance, but they surely have merit. Like the far south, the high north is no longer a place of interest to only a select few. Nations in the Arctic Circle will rightly insist on having the biggest say, but all interested countries should at least be offered a voice. And to avoid polluting the Arctic is a cause behind which everyone can surely unite. ■

Damage limitation

Spider webs are designed to cope with stress and disruption, favouring repair over rebuilding.

With a proposed referendum on Scottish independence likely to happen in 2014, some 700 years after the Scots army triumphed over English forces at the symbolic Battle of Bannockburn, one tale that seems certain to be told in the build-up is the story of Scotland's King Robert the Bruce and the spider. According to legend, Bruce was hiding in a cave in the wake of several defeats when he was inspired to fight again after watching a spider persevere, and eventually succeed, in its repeated attempts to spin a web.

As Bruce — who led the Scots to victory at Bannockburn — discovered, failure does not come easily to a spider. And although the amazing properties of spider silk have fascinated us for generations, the secrets of their webs have remained elusive.

In a paper on page 72 of this issue, Markus Buehler at the Massachusetts Institute of Technology in Cambridge and his colleagues report on perhaps the most impressive design feature of a spider's web: its structural and mechanical strength. In research that both modelled webs and investigated those spun *in situ* by local garden spiders, the authors found that the strands of silk adapt to the amount of stress they experience, and how that stress is loaded onto them.

Under a light stress, a gentle highland breeze perhaps, the silk softens and extends, so allowing the web to retain its structure. But when a larger and more disruptive force strikes — such as a hand groping for a light switch in a dark attic — the silk strands first extend, then the most stretched of those strands become suddenly rigid and so break. This sacrifice of a strand or two localizes the damage, and keeps the rest of the web intact. Once the disturbance has passed, the spider can scurry out to repair the web, rather than being forced to rebuild. As Bruce — who exploited heavily wooded areas to conceal his preparations for the decisive battle — discovered, it is easier to persevere, and to succeed, when nature is on your side.

These are heady times for arachnophiles. Last month, a stunning shawl and cape woven from spider silk went on display at London's Victoria and Albert Museum. The two garments, which took eight years to create, contain silk produced by more than one million female Madagascan golden orb-weaver spiders, amassed by a team of 80 people. They used long poles to collect the spiders from their webs each day, and harvested their silk before returning them to the wild. The garments are the first textiles to be made from spider silk since a set of bed hangings displayed at the 1900 Paris Exhibition. It is another achievement for the power of perseverance. Or perhaps, as those set to campaign in 2014 for Scotland to remain part of the United Kingdom might stress, it marks a triumph of, and a tribute to, sticking together. ■

➲ NATURE.COM
To comment online, click on Editorials at: go.nature.com/xhunqv

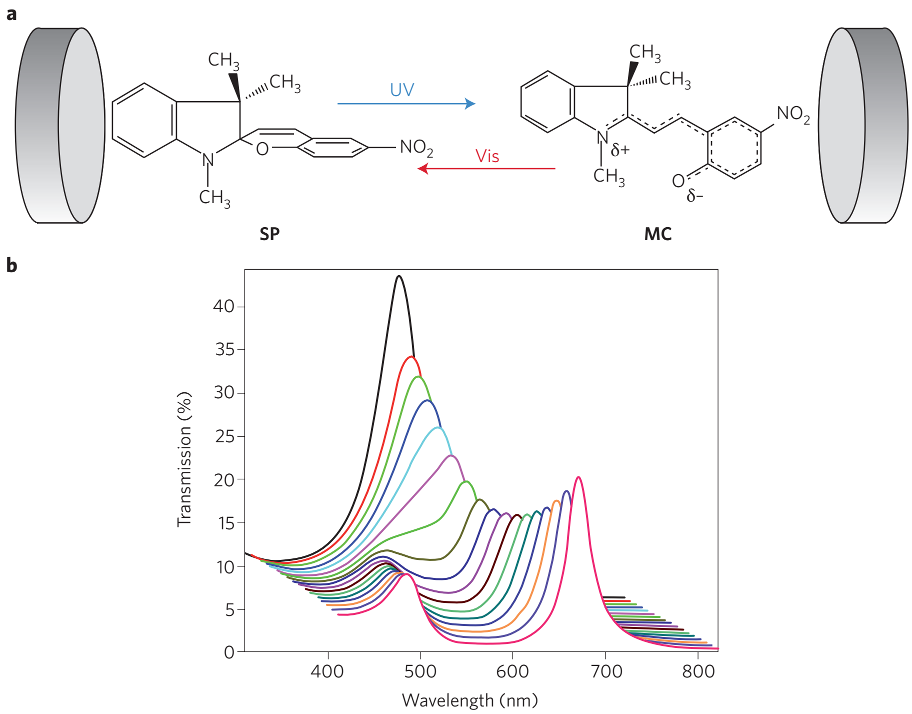

Figure 2 | Achieving strong coupling. **a**, Schematic of the photochromic conversion between merocyanine (MC) and spiropyran (SP) occurring in an optical cavity. **b**, Transmission spectrum of the coupled system formed by the cavity and the photochromic molecules. The initial (black) spectrum corresponds to the SP molecules, not in resonance with the cavity mode. By exposing SP molecules to 330 nm light, they are converted into MC molecules thereby entering in resonance with the cavity. As the concentration of MC increases, a transition from weak (for example, light blue curve) to strong (for example, violet curve) and eventually ultrastrong (for example, dark pink curve) coupling occurs. A key observation is that the separation between the two new bands increases with irradiation time. Figure reproduced with permission from ref. 3, © 2012 Wiley.

sensing. One of the most exciting parts of this research comes from the fact that these states are highly cooperative among many molecules, hence it is legitimate to ask what would the transport properties be through these states? Are they similar to band states? If not, what are the differences? What is the real nature of the coupling between the split states?

Finally, an intriguing fact is highlighted by Ebbesen and colleagues[3]: ultrastrong coupling also exists in the absence of light, and can occur only as an effect of vacuum fluctuations of the electromagnetic field. This suggests a link between ultrastrong coupling, Casimir and van der Waals forces. Do these molecules exert a force on the cavity just by being there, and if so, is this another form of Casimir force, a resonant one? ❐

Anna Fontcuberta i Morral and Francesco Stellacci are at the Institute of Materials, École Polytechnique Fédérale de Lausanne, CH-1015 Lausanne, Switzerland.
e-mail: francesco.stellacci@epfl.ch

References

1. Rodrigez, A. W., Capasso, F. & Johnson, W. G. *Nature Photon.* **5,** 211–221 (2011).
2. Schwartz, T., Hutchison, J. A., Genet, C. & Ebbesen, T. W. *Phys. Rev. Lett.* **106,** 196405 (2011).
3. Hutchison, J. A., Schwartz, T., Genet, C., Devaux, E. & Ebbesen, T. W. *Angew. Chem. Int. Ed.* **51,** 1592–1596 (2012).
4. Geddes, C. D. & Lakowicz, J. R. *J. Fluoresc.* **12,** 121–129 (2002).
5. Nie, S. M. & Emery, S. R. *Science* **275,** 1102–1106 (1997).
6. Purcell, E. M. *Phys. Rev.* **69,** 681 (1946).
7. Hood, C. J., Chapman, M. S., Lynn, T. W. & Kimble, H. J. *Phys. Rev. Lett.* **80,** 4157–4160 (1998).
8. Reithmeier, J. P. *et al. Nature* **432,** 197–200 (2004).
9. Savona, V. *et al. Solid State Commun.* **93,** 733–739 (1995).
10. Haroche, S. & Kleppner, D. *Phys. Today* **42,** 24–30 (January 1989).
11. Yoshie, T. *et al. Nature* **432,** 200–203 (2004).
12. Lidzey, D. G. *et al. Nature* **395,** 53–55 (1998).
13. Lukyanchuk, B. *et al. Nature Mater.* **9,** 707–715 (2010).
14. Hao, F. *et al. Nano Lett.* **8,** 3983–3988 (2008).
15. Ciuti, C., Bastard, G. & Carusotto, I. *Phys. Rev. B* **72,** 115303 (2005).
16. De Liberato, S., Ciuti, C. & Carusotto, I. *Phys. Rev. Lett.* **98,** 103602 (2007).
17. Niemczyk, T. *et al. Nature Phys.* **6,** 772–776 (2010).

SPIDER WEBS

Damage control

A study reveals that spider orb webs fail in a nonlinear fashion, owing to the hierarchical organization of the silk proteins. The discovery may serve as inspiration for engineers for the design of aerial, light-weight, robust architectures.

Fiorenzo G. Omenetto and David L. Kaplan

Spider orb webs are notable feats of materials engineering. Their mechanical functions, optimized over 400 million years of evolution, have prompted strong interest among physical scientists and engineers in understanding, mimicking and extending the design of such a remarkable natural architecture for the fabrication of light-weight, aerial structures.

In a recent paper published in *Nature*, Markus Buehler and collaborators[1] offer useful insights into the relationship between structure and function in orb webs with regard to the hierarchical structure of silk proteins. Through a combination of modelling and experiments, they show that the mechanical properties of spider-silk fibres and webs are due to a nonlinear response to strain of the individual threads. This nonlinear behaviour has the favourable effect of localizing failures in specific regions of the orb web on impact by a flying prey. (A linear elastic — or elastic–plastic — response would not provide this buffering protection and would lead to failure of the whole structure.)

But just how does this nonlinear response come about from the proteic

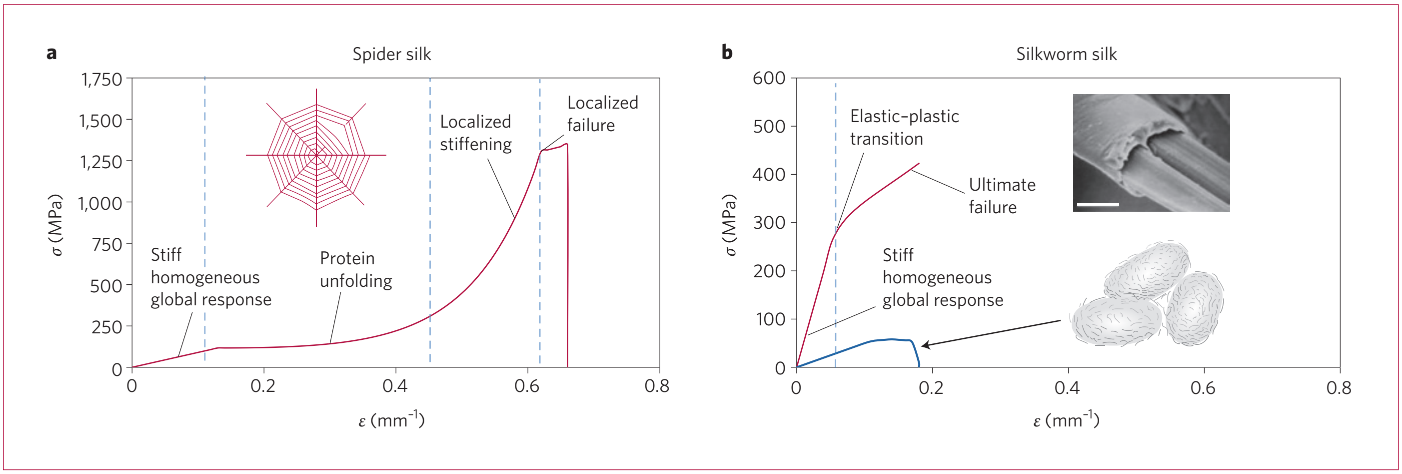

Figure 1 | Species-specific mechanical behaviour of silk fibres under tensile loading. **a**, Theoretical stress (σ)–strain (ε) plot for a spider-silk fibre showing the various phases of load response[1]. Inset: spiders exploit the nonlinearity of their silk fibres to localize web damage. **b**, Experimental data of silkworm-silk fibre fibroin (red)[5] and cocoons (blue)[6]. Inset: SEM image of a silkworm fibre composite used in a cocoon[5] showing fibroin fibres embedded in a softer cladding. Scale bar, 5 µm. This morphology results in poor tensile stiffness of the cocoons. Unlike spiders, silkworms exploit their silk for impact toughness and protection. SEM image reproduced from ref. 5, © 2002 NPG.

structure of silk? The answer relates to the primary sequence of silk proteins, where intra- and interchain structures generate nanodomains that include crystalline β-sheet regions that undergo reorientation and unfolding at low levels of stress. As stress increases, these crystalline regions respond by forming hydrogen bonds, locally stiffening the structure. Further stress results in thread failure (Fig. 1a). It is this nonlinear stiffening behaviour that produces localized damage, thus allowing the rest of the structure to retain its function.

It is remarkable that the optimized mechanical properties of individual spider-silk fibres can be translated into complex web architectures. The function and resiliency of the web embodies a compromise between linear softening and successive stiffening of the individual fibres, providing control of local versus global failure of the web structure. This design allows the web to continue to function despite the loss of large segments of its structure. It is important to note that global web failure would represent an evolutionary disadvantage for the spider, owing to its inability to capture prey and the metabolic penalty involved in web reconstruction.

The findings of Buehler *et al.*[1] are based on insights by Vollrath and colleagues[2], who observed that web structures exhibited time-dependent stress–strain responses on impact of a flying insect. According to this model, pre-tensioned stiff radial threads dominate web properties, whereas the less stiff spiral threads provide differences in radial versus circumferential stiffness, allowing aerodynamic damping of the web and capture of the insect.

The nonlinear behaviour of spider webs is different from that of silkworm cocoons — egg-shaped structures designed to protect insect larvae from the external environment. Silkworm cocoon fibres are made of protein–protein composites that dissipate stress through a linear elastic–plastic deformation. This type of response acts on the whole structure of the cocoon, improving its fracture toughness and therefore the chances of survival of the moulting animal housed inside. The difference between silkworm-silk fibres and spider-silk fibres originates from the primary amino acid sequence in the respective proteins. Silkworm-silk fibres possess a significantly higher content of crystalline domains than spider-silk fibres, thus dampening some of the nonlinear response observed in spider orb webs (Fig. 1b).

Current materials engineering design ideas are at the early stages for light-weight composite structures. The focus of such designs is typically on mechanical performance and manufacturability, whereas both mechanical functions and energetic limitations must be considered concurrently. In this respect, spider silks can serve as a model and inspiration owing to their unique design that is optimized for mechanics, yet constrained by energy budgets. Further interest in this natural material is driven by the complete recyclability and degradability of the fibres as well as the environmentally friendly preparation process[3].

Other natural materials, such as ligaments and tendons, also exhibit nonlinear elastic behaviour[4]. In a broader perspective, this paradigm could extend to the design of biomaterial systems for cell and tissue studies. Evolving nonlinear stress–strain mechanical functions are relevant during tissue development, where patterning, stress distribution, and associated biological signalling are critical to prevent premature catastrophic failures such as abnormal tissue development. The ability to design material structures with local modes of failure, or perhaps regions that become more accessible to specific cells or enzymes on deformation, could define a biomaterials platform with topographic control of functions. To this end, the combined use of *in situ* experiments and modelling may redefine design rules that would incorporate the tenets of naturally occurring materials for materials engineering purposes. ❐

Fiorenzo G. Omenetto and David L. Kaplan are in the Department of Biomedical Engineering of Tufts University, Medford, Massachusetts 02155, USA. e-mail: david.kaplan@tufts.edu; fiorenzo.omenetto@tufts.edu

References

1. Cranford, S. W., Tarakanova, A., Pugno, N. M. & Buehler, M. J. *Nature* **482,** 72–76 (2012).
2. Lin, L. H., Edmonds, D. T. & Vollrath, F. *Nature* **373,** 146–148 (1995).
3. Omenetto, F. G. & Kaplan, D. L. *Science* **329,** 528–531 (2010).
4. Altman, G. H. & Horan, R. L. in *An Introduction to Biomaterials* (eds Guelcher, S. A. & Hollinger, J. O.) 499–524 (CRC, 2006).
5. Shao, Z. Z. & Vollrath, F. *Nature* **418,** 741 (2002).
6. Chen, F., Porter, D. & Vollrath, F. *Phys. Rev. E* **82,** 041911 (2010).